Algebraic Dynamic Multilevel Simulation of Coupled Flow and Heat Transfer in Heterogeneous Geothermal Reservoirs with Fluid-Rock Non-Thermal Equilibrium Effects

Rhadityo Bhaskoro Arbarim

Student ID: 4573900

Technische Universiteit Delft

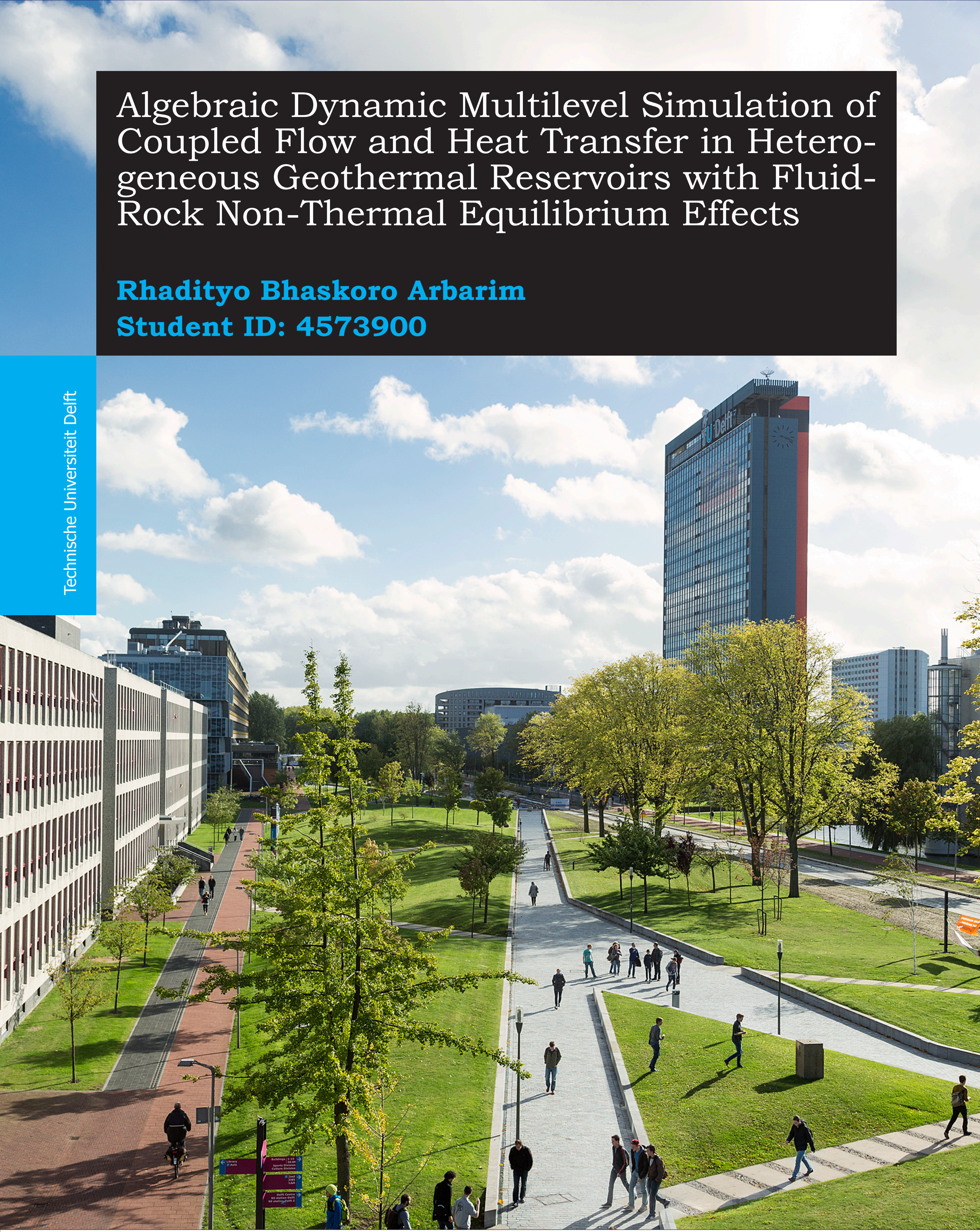

TU Delft
Delft
University of
Technology

Challenge the future

Algebraic Dynamic Multilevel Simulation of Coupled Flow and Heat Transfer in Heterogeneous Geothermal Reservoirs with Fluid-Rock Non-Thermal Equilibrium Effects

by

Rhadityo Bhaskoro Arbarim
Student ID: 4573900

to obtain the degree of Master of Science
at the Delft University of Technology,
to be defended publicly on Tuesday August 30, 2018 at 14:00 AM.

Student number:	4573900	
Project duration:	November 1, 2017 – August 30, 2018	
Thesis committee:	Dr. Hadi Hajibeygi,	TU Delft, supervisor
	Dr. William R. Rossen,	TU Delft
	Dr. Anne-Catherine Dieudonné,	TU Delft

This thesis is confidential and cannot be made public until December 31, 2018.

An electronic version of this thesis is available at `http://repository.tudelft.nl/`.

Abstract

Accurate simulation of fluid flow and heat transfer in geothermal reservoirs is a crucial necessity for optimising energy extraction strategies. However, natural formations (including geothermal ones) extend large length scales (in the order of km), while their properties (e.g., heat and flow conductivity) can change in small (fine) scales (e.g., cm or even below). As such, accurate simulations of filed-scale models are too expensive to be handled by the state-of-the-art commercial simulators. As a matter of fact, these geological models are upscaled excessively in order to reduce the computational costs. Excessive upscaling leads to loss of accuracy and details of the heterogeneous properties, which can result in non-optimum production estimation and operation strategies. As a remedy, in this work, we propose a dynamic multilevel method (ADM) which captures small-scale heterogeneity (i.e., accurate) while preserving the computational efficiency (thus applicable to field-scale models). This development is achieved by combining two major concepts: (1) multiscale basis functions for accurate coarse-scale treatment of heat and flow conductive properties at their original fine-scale, and (2) adaptive mesh refinement strategy to minimise the requirement for employing the fine-scale grid, i.e., when and where needed. These two developments combined in one framework allows for both accurate and efficient simulation of coupled flow-heat equations in subsurface geothermal reservoirs. The fine-scale grid is employed only at the cold water front, where most of the nonlinear (and grid resolution sensitive) interaction is taking place. The rest of the domain is solved at the coarser scales, depending on the gradients (slope of change) of the unknowns. Note that no upscaling is needed due to the employment of multiscale basis functions. Moreover, these basis functions are calculated only once at the beginning and reused for the rest of the time-dependent simulations. Our method allows for non-thermal equilibrium between rock and injected fluid, so to allow for full flexibility and possible added accuracy. Through several test cases, the accuracy of the proposed ADM is investigated by measuring its error compared with the fine-scale fully resolved simulation. Its accuracy, on the other hand, is measured through calculating the average number of active grid cells. Our results, for both homogeneous and heterogeneous models, show that the proposed method employs a fraction of the fine-scale grids to deliver accurate solutions. Therefore, it provides a promising framework for field-scale simulation of geothermal reservoirs.

Preface

Firstly, I would like to thank The Almighty God who bestows me with His eternal blessing and guidance, so that I manage to conclude my thesis work at a perfect moment.

With title **Algebraic Dynamic Multilevel Simulation of Coupled Flow and Heat Transfer in Heterogeneous Geothermal Reservoirs with Fluid-Rock Non-Thermal Equilibrium Effects**, this thesis work is designated to obtain Master of Science degree in Petroleum Engineering and Geoscience Department at Technische Universiteit Delft.

Upon finalisation of this thesis, the author grants numerous helps and supports on many occasions. Therefore, the author would like to send sincere thanks to

1. My dearest woman in the world, Pamila Adhi Annisa, for your tremendous unconditional love and affection.
2. My dearest family in Magelang and Jakarta who have been looking after me and raising me the since I was born and still counting.
3. Dr Hadi Hajibeygi as my superb advisor who always challenges me with constructive discussion and criticism as well as your insight regarding my academic career.
4. Mousa HosseiniMehr and Matteo Cusini as my technical advisor. Without you, I could have spent much longer time when implementing in DARSim2 code. You are such helpful and friendly man.
5. *Lembaga Pengelola Dana Pendidikan* (LPDP) Indonesia for the financial support during entire two years of my study in TU Delft.

Last but not least, this thesis work is however still far from perfection. Any comments and criticism are kindly welcome to improve the quality of the thesis work.

Author
Rhadityo Bhaskoro Arbarim
30, August 2018

Contents

Abstract iii

Preface v

List of Figures ix

1 Introduction 1
- 1.1 Heat Transfer in Geothermal Reservoir 2
  - 1.1.1 Conduction 2
  - 1.1.2 Convection. 2
- 1.2 Algebraic Dynamic Multilevel (ADM) 3
- 1.3 Research Objectives. 3

2 Governing Equations 5
- 2.1 Mass Balance Equation 5
- 2.2 Energy Balance of the Fluid Body 5
- 2.3 Energy Balance of the Rock Body 6

3 Simulation Strategy 7
- 3.1 Discretisation 7
  - 3.1.1 Mass Balance 7
  - 3.1.2 Energy Balance of the Fluid Body 8
  - 3.1.3 Energy Balance of the Rock Body. 8
- 3.2 Solution Strategy 9

4 Algebraic Dynamic Multilevel (ADM) 13
- 4.1 MSFV Operator Builder 13
- 4.2 ADM Solution Strategy 14
- 4.3 Selection of ADM Grid 15

5 Result and Discussion 17
- 5.1 Case 1 : Homogeneous Reservoir 18
- 5.2 Case 2 : Blocky-Homogeneous Reservoir 20
- 5.3 Case 3 : Patchy-Heterogeneous Reservoir 22
- 5.4 Case 4 : Channelized-Heterogeneous Reservoir 24
- 5.5 Case 5 : Anisotropic-Heterogeneous Reservoir 26

6 Conclusion 29

A Fluid and Rock Properties 31

Bibliography 33

List of Figures

1.1 Heat conduction on 1D plate. The slope of temperature distribution defines the conduction coefficient. 2
1.2 Two types of convection on 1D fluid and solid boundary. 3
1.3 ADM grids resolve part of the domain with significant change in fine-scale resolution and solve the rest in multilevel grids [1]. 3

3.1 Illustration of discretisation in 2D domain. 7
3.2 Flowchart of fully implicit geothermal reservoir simulator in fine-scale resolution. Subscript 0 indicates fine-scale resolution 11

4.1 Example of 2D multiscale grids consists of 15 × 15 fine-scale resolution. 13
4.2 Flowchart of fully implicit geothermal reservoir simulator in ADM resolution. Note that the algorithm involves static prolongation and restriction operators. 16

5.1 Solution after 250 days of injection in homogeneous reservoir. Fine-scale solution (left) is approximated by ADM solution (right) with $\delta T = 10\%$ corresponding to 17% of active grids. 18
5.2 Solution after 750 days of injection in homogeneous reservoir. Fine-scale solution (left) is approximated by ADM solution (right) with $\delta T = 10\%$ corresponding to 17% of active grids. Note that diffused temperature front is sufficiently captured by coarser grids. 19
5.3 Test Case 1 : Error of ADM solution with respect to fine-scale reference (a) and percentage of ADM active grids as function of ADM tolerance (b), and history of ADM grids during simulation (c). 19
5.4 Test Case 1 : Absolute temperature difference of fluid and rock [K] after 0.01 (a), 0.1 (b), 1 (c), and 10 (d) days of injection. 20
5.5 Blocky-homogeneous permeability field [m^2] used in test case 4. 20
5.6 Solution after 200 days of injection in blocky-homogeneous reservoir. Fine-scale solution (left) is approximated by ADM solution (right) with $\delta T = 10\%$ corresponding to 35% of active grids at the end of simulation. 21
5.7 Test Case 2 : Error of ADM solution with respect to fine-scale reference (a) and percentage of ADM active grids as function of ADM tolerance (b), and history of ADM grids during simulation (c). 21
5.8 Test Case 2 : Absolute temperature difference of fluid and rock [K] after 0.01 (a), 0.1 (b), 1 (c), and 10 (d) days of injection. 22
5.9 Heterogeneous permeability field [m^2] extracted from SPE10 top layer permeability database. . . 22
5.10 Solution after 65 days of injection in patchy-heterogeneous reservoir. Fine-scale solution (left) is approximated by ADM solution (right) with $\delta T = 10\%$ corresponding to 37% of active grids. . . 23
5.11 Test Case 3 : Error of ADM solution with respect to fine-scale reference (a) and percentage of ADM active grids as function of ADM tolerance (b), and history of ADM grids during simulation (c). 23
5.12 Test Case 3 : Absolute temperature difference of fluid and rock [K] after 0.01 (a), 0.1 (b), 1 (c), and 10 (d) days of injection. 24
5.13 Heterogeneous permeability field [m^2] extracted from SPE10 bottom layer permeability database. 24
5.14 Solution after 75 days of injection in channelized-heterogeneous reservoir. Fine-scale solution (left) is approximated by ADM solution (right) with $\delta T = 10\%$ corresponding to 43% of active grids. 25
5.15 Test Case 4 : Error of ADM solution with respect to fine-scale reference (a) and percentage of ADM active grids as function of ADM tolerance (b), and history of ADM grids during simulation (c). 25

5.16 Test Case 4 : Absolute temperature difference of fluid and rock [K] after 0.01 (a), 0.1 (b), 1 (c), and 10 (d) days of injection. 26
5.17 Solution after 50 days of injection in anisotropic-heterogeneous reservoir. Fine-scale solution (left) is approximated by ADM solution (right) with δT = 13% corresponding to 38% of active grids. 26
5.18 Test Case 5 : Error of ADM solution with respect to fine-scale reference (a) and percentage of ADM active grids as function of ADM tolerance (b), and history of ADM grids during simulation (c). 27
5.19 Test Case 5 : Absolute temperature difference of fluid and rock [K] after 0.01 (a), 0.1 (b), 1 (c), and 10 (d) days of injection. 27

1

Introduction

Global warming has become one of the primary concerns in modern industry. High dependency of global industry on fossil fuels has lead to massive carbon emission. As a result, 1^{o}C increase in the Earth temperature was observed over the past century [2] and claims 47 to 139 GT mass loss of West Antarctica ice sheet annually within the time frame of 1992 to 2006 [3]. A recent study estimates that global Antarctic melting contributes up to one meter sea level rise by 2100 [4].

As the concerns about the adverse effect of burning fossil fuels increases, the world, therefore, is in urgent need of a cleaner alternative source of energy [5]. With its capacity to supply 17% of world population [6] and CO_2 emission 20 – 35 g/kWh or 30 times smaller than the one from coal [7], geothermal energy is seen as a promising future energy supply to reduce carbon emission and is expected to provide larger contribution to meet energy demands [8–10].

Geothermal reservoir is considered as a giant heat exchanger where the energy can be collected from natural hot springs or by harvesting the heat stored in hot dry rock formation. Hot dry rock is referred to as underground formation rock which lies 3 km below surface with temperature at least 200^{o}C [11, 12] and possesses more than 70% of the available energy [13]. As such, the existing thermal equilibrium assumption which presumes rock and fluid have common temperature [14] might fail under complex physical-configuration [15].

Like common geological features, a geothermal reservoir can extend hundreds or even thousands of meters while including high heterogeneity contrasts over small distances, which can lead to non-uniform temperature distribution [13]. Along with the necessity of employing high resolution grids, the linear and nonlinear stability of the resulting coupled discrete systems can significantly influence simulator performance [16].

In this work, a scalable framework for field-scale simulation of the geothermal reservoirs is described. It is aimed to be a powerful tool to simulate thermal flow in heterogeneous geothermal reservoirs, with no upscaling of the underlying fine-scale heterogeneity. The fine-scale system is obtained by using the fully-implicit integration scheme where mass and energy balance, or so-called flow-heat, are coupled to obtain pressure, fluid temperature, and rock temperature. The mentioned strong non-linearity is linearized using Newton-Raphson linearization lemma. Note that the performance of linear solver depends strongly on correct simulation strategy. In the presence of strong non-linear flow-heat coupling, appropriate preconditioning— i.e., constrained pressure residual (CPR) methods and their extensions—is an essential requirement to the success of the nonlinear solver [17, 18].

The obtained fine-scale fully implicit system, which is computationally expensive, has been typically upscaled to lower resolution systems in order to be solved efficiently with a commercial simulator. This leads to loss of accuracy, and no control of the error with respect to the fine-scale fully resolved system. To resolve this challenge, here, we propose an alternative approach with maintains its computational efficiency as the problem size gets bigger, and, at the same time, it resolves the fine-scale heterogeneity. In addition, it allows for error control and reduction to the desired level with respect to the fine-scale fully resolved system. The proposed method is called “Algebraic Dynamic Multilevel (ADM)” [1, 19]. In this work, the first ADM method for geothermal reservoirs is developed and presented.

This development is achieved by combining two major concepts: (1) multiscale basis functions for accurate coarse-scale treatment of heat and flow conductive properties at their original fine-scale, and (2) adaptive mesh refinement strategy to minimise the requirement for employing the fine-scale grid, i.e., when and where needed. While the first item targets the global components of the solution space, the adaptive grid refinement (i.e., the second item) is targeted for the local component of the solution (i.e., sharp fronts of the transport equation). These two developments combined in one framework allows for both accurate and efficient simulation of coupled flow-heat equations in subsurface geothermal reservoirs. Such a method allows one to dynamically select coarsening level on the basis of front-tracking criterion, where sub-domain with steep gradient is resolved in fine-scale resolution, whilst the rest of the domain is resolved in hierarchical nested resolution.

The development of this work is firstly started with revisiting mass and energy balance equations as the foundation of geothermal reservoir simulation, as discussed in chapter 2 and followed by numerical discretization of the governing equations and coupling strategy in chapter 3. Multiscale and Algebraic Dynamic Multilevel (ADM) strategy will be presented in chapter 4 followed by numerical simulation result in chapter 5. Finally, the project is concluded by recommendation and conclusions as shown in chapter 6.

1.1. Heat Transfer in Geothermal Reservoir

Heat in general can be transferred in three ways (i.e., conduction, convection, and radiation). In geothermal reservoir models, heat transfer from conduction and convection are considered. The effect of radiation, or heat transfer carried by electromagnetic waves, is typically neglected.

1.1.1. Conduction

Conduction can take place in any phase including gas, liquid, and solid which is caused by increase of internal energy from colliding particles (i.e., atoms and electrons) in microscopic scale. As such, an object with higher temperature has more molecular activities thus is able to transmit energy to less energetic object.

Analogous to Darcy's and Fick's law, Jean Baptiste Joseph Fourier in [20] states that conduction occurs if two bodies with temperature difference are in physical contact. In addition, thermal conductivity proportionally influences conductive heat transfer. The value of thermal conductivity varies in smaller degree compared to permeability [21]. Figure 1.1 illustrates heat transfer by conduction.

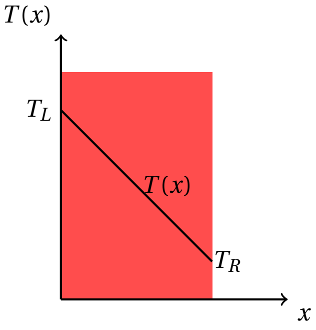

Figure 1.1: Heat conduction on 1D plate. The slope of temperature distribution defines the conduction coefficient.

1.1.2. Convection

Convection is heat transfer mechanism by macroscopic fluid movement which can be classified on the basis of the driving force of the fluid movement. Free or natural convection refers to fluid movement by buoyancy force, whereas forced convection refers to fluid movement which mechanically driven by external force.

Generally, convection comprises two mechanisms: diffusion and advection. Diffusion mechanism takes place between solid and moving fluid. Here, contact area and temperature difference play major role in determining magnitude of diffusion [22].

Advection, on the other hand, refers to transport of energy via bulk motion of the fluid. Unlike conduction, advection takes place only in fluid phase since it requires fluid currents to carry conserved quantity. Figure 1.2 illustrates two mechanism of convective heat transfer.

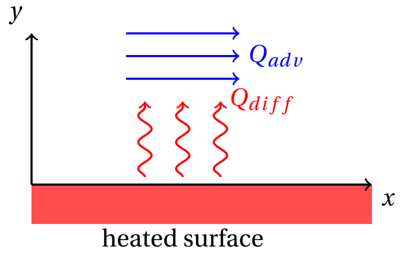

Figure 1.2: Two types of convection on 1D fluid and solid boundary.

1.2. Algebraic Dynamic Multilevel (ADM)

The geological properties of geothermal reservoir is often heterogeneous at fine resolution. Compared to the size of the geothermal reservoirs (order of km), capturing all these heterogeneities and physical processes would require fine-scale grids beyond the scope of reservoir simulators. Due to size of the resulting linear systems, real field-scale simulations become computationally too expensive. One solution to tackle this challenge is to upscale the properties and reduce the size of the linear system. Unfortunately, using excessively upscaled quantities can result in loss of accuracy. This motivates the development of advanced methods which provide accurate and efficient results, applicable to real-field models.

The multiscale methods were developed to provide accurate solutions for flow in heterogeneous porous media, by solving a linear system in coarse scale and then mapping it back to fine-scale [23–26] with the help of prolongation and restriction operators. Elliptic part of the mass balance equation is used to construct local basis functions [27, 28]. Other types of prolongation operators (namely constant and bilinear) can also be seen as basis functions with constant and bilinear solutions [23, 29].

Algebraic Dynamic Multilevel (ADM) method, which is derived from the combination of multilevel multiscale methods with dynamic grid refinement strategy [30–33], allows one to resolve parabolic-hyperbolic system of equations. Once extended to single phase geothermal reservoirs, i.e., in this work, it would provide an efficient solution while maintaining accuracy, based on employment of high-resolution grids only when and where it is needed [1]. It dynamically changes the grid size if satisfies a coarsening criterion and allows one to resolve in nested hierarchical grids.

The coarsening level of nested ADM grids is dynamically selected by temperature coarsening criterion. ADM method aims to preserve accuracy in reasonably low computational cost. Temperature front is captured in fine-scale resolution while the rest of the domain is solved on coarser levels. Note that this work is limited to structured grids. On complex reservoir-geometry with unstructured grid, unstructured multiscale basis functions are required to allow unstructured ADM [34–36]. Figure 1.3 shows example of ADM grid configuration in structured grids.

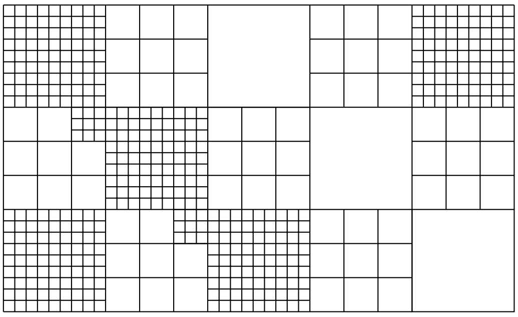

Figure 1.3: ADM grids resolve part of the domain with significant change in fine-scale resolution and solve the rest in multilevel grids [1].

1.3. Research Objectives

In this work, for the first time, ADM method for simulation of coupled flow-heat equations in heterogeneous geothermal reservoirs is developed. The development is based on a fully-coupled treatment of the nonlinear coupling between the flow and heat transfer, to resolve the convergence difficulties reported in the recent literature [37].

This research includes further development of geothermal simulators and extends multiscale methods for coupled flow and heat [38] with signfiicant improvements. The primary goals of this research are as the following.

1. Verifying applicability of thermal equilibrium assumption in non-fractured reservoirs.
2. Formulating fully implicit method (FIM) to couple flow and heat problem in geothermal reservoirs.
3. Developing ADM method for coupled flow and heat transfer problem in heterogeneous porous media.
4. Implement the developed method in DARSim2 and investigate its performance.

The first two items above have been developed with MATLAB code from scratch, while the last two items have been formulated and implemented in the existing TU Delft in-house DARSim2 simulator. As such, the developments of this project will stay in the DARSim research group for future use and extensions.

2

Governing Equations

Geothermal reservoir simulation, under single-phase flow regime, consists of two main equations to be solved for pressure and temperature. Pressure solution is obtained from mass balance equation, whereas temperature solution is derived from energy balance equation. In geothermal terminology, both equations are often called flow and heat equation, respectively. Note that if the fluid and rock temperature values are different, then 2 equations for temperatures need to be solved.

This chapter describes the continuum formulation for flow and heat transfer in heterogeneous geothermal reservoirs.

2.1. Mass Balance Equation

In an arbitrary control volume Ω, mass conservation equation can be expressed as

$$[\text{mass accumulation}] + [\text{net mass flux}] = [\text{mass source over } \Omega]. \tag{2.1}$$

In the limit of small Ω, after some mathematical manipulations, equation (2.1) leads to a differential equation, i.e.,

$$\frac{\partial(\phi\rho)}{\partial t} - \nabla\cdot\left(\rho\lambda\nabla P\right) = \rho q^w \quad \text{on} \quad \Omega^m, \tag{2.2}$$

where ϕ is matrix porosity, ρ represents fluid density, μ denotes fluid viscosity and λ is fluid mobility $\left(\lambda = \frac{k}{\mu}\right)$.

Unlike conventional oil reservoir, viscosity of the fluid in geothermal reservoirs cannot be assumed constant, yet it changes as a function of temperature. Meanwhile, density has dependency on both pressure and temperature. Therefore, $\rho = f(P, T)$ and $\mu = f(T)$. Both properties are calculated using the formulations presented in appendix A.

Well volumetric flow rate q^w is calculated in discrete form (when grid sizes are known) using Peaceman model [39] and reads

$$q^w = \mathrm{PI}\,\lambda\left(P^w - P\right), \tag{2.3}$$

where PI and P^w denote well productivity index and borehole pressure, respectively.

2.2. Energy Balance of the Fluid Body

With no gravitational nor kinetic energy, the energy balance in geothermal reservoir can be formulated only by taking energy from heat into account. In an arbitrary control volume Ω, energy conservation equation in fluid body can be expressed as

$$\left[\text{energy accumulation}\right] + \left[\text{transport of energy}\right] + [\text{net conductive heat transfer}] = [\text{heat source over } \Omega]. \tag{2.4}$$

In addition, conductive heat flow is far less significant than advective heat flow ($E_{cond} \ll E_{adv}$), thus negligible. Fluid energy balance for single phase geothermal reservoir can be written in differential form as

$$\frac{\partial\left(\phi\rho C_p T\right)}{\partial t} - \nabla\cdot\left(\rho h\lambda\cdot\nabla P\right) = \rho h q^w + Q_h^{fr} \quad \text{on} \quad \Omega^m \tag{2.5}$$

for fluid temperature T, where h is fluid enthalpy and C_p is fluid specific heat. Note that well energy flux is proportional to multiplication of enthalpy and well mass flux.

The last term of equation (2.5) indicates diffusive heat transfer. The term diffusive heat transfer physically refers to heat exchange between solid and fluid phase of the reservoir. Fluid-rock heat exchange is calculated using Newton's law of cooling [22, 40] and reads

$$Q_h^{fr} = AU\left(\overline{T} - T\right), \tag{2.6}$$

where A is contact area between pore and matrix, U is overall heat transfer coefficient, and $\overline{T}$ is the rock temperature.

2.3. Energy Balance of the Rock Body

Heat transfer inside the solid part of the medium occurs mostly by the means of conduction. Note that the conduction in this work is limited only within reservoir boundary. In an arbitrary control volume Ω, energy conservation in solid part of the reservoir reads

$$\left[\text{energy accumulation}\right] + [\text{net conductive heat transfer}] = [\text{heat source over } \Omega], \tag{2.7}$$

which is equivalent in differential form to

$$\frac{\partial\left((1-\phi)\,\overline{\rho}\,\overline{C}_p\,\overline{T}\right)}{\partial t} - \nabla\cdot\left(k_r\nabla\overline{T}\right) = Q_h^{rf} \quad \text{on} \quad \Omega^m. \tag{2.8}$$

Here, $\overline{\rho}$ and $\overline{C}_p$ are density and specific heat of the rock. Note that to ensure energy conservation, the energy leaves from rock matrix must be equal to the energy received by the fluid. Fluid-rock heat exchange couples fluid and rock domain and is defined in strictly conservative way

$$\int Q_h^{rf}\,d\Omega = -\int Q_h^{fr}\,d\Omega\,. \tag{2.9}$$

3

Simulation Strategy

The focus of this chapter is to solve the equations in order to find the unknowns. From continuum form in chapter 2, the equations are then transformed into discrete form in section 3.1 with finite volume scheme for spatial domain, and Euler backward for time discretisation. The obtained discrete form is then solved using Fully Implicit Method (FIM), as described in section 3.2.

3.1. Discretisation

To describe discrete forms from all governing equations, consider the example of a 2D domain as pictured in figure 3.1. Note that finite-volume method and Euler backward are employed for spatial and temporal discretisation, respectively. Also note that the fluid properties are discretised with upwind scheme.

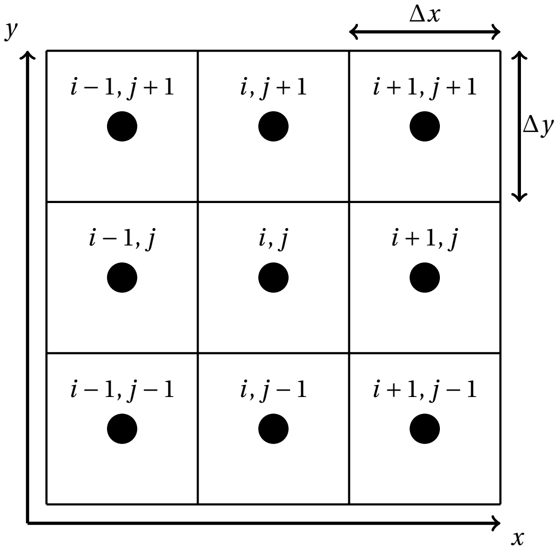

Figure 3.1: Illustration of discretisation in 2D domain.

3.1.1. Mass Balance

Equation (2.2) can be rewritten in discrete form, integrated over control volume and given by

$$\int \frac{(\phi\rho)^{n+1} - (\phi\rho)^{n}}{\Delta t} d\Omega - \int \nabla \cdot \left(\rho\lambda\nabla P\right)^{n+1} d\Omega = \int \rho q^{w} d\Omega, \tag{3.1}$$

where the second term on LHS indicates net mass flow over control volume. Applying Gauss divergence theorem on divergence term and substituting back into equation (3.1) reads

$$\int \frac{(\phi\rho)^{n+1} - (\phi\rho)^{n}}{\Delta t} d\Omega - \oint_{\Gamma} n \cdot \left(\rho\lambda\nabla P\right)^{n+1} d\Gamma = \int \rho q^{w} d\Omega. \tag{3.2}$$

Equation (3.2) is non-linear due to pressure dependency of porosity and density. Residual form of equation (3.2) reads

$$r_m^{n+1} = \int \rho q^{mw} d\Omega - \int \frac{(\phi\rho)^{n+1} - (\phi\rho)^n}{\Delta t} d\Omega + \oint_\Gamma n \cdot \left(\rho\lambda\nabla P\right)^{n+1} d\Gamma, \tag{3.3}$$

which indicates mass conservation if r_m^{n+1} is equal to zero. In discrete form, equation (3.3) can be written as

$$\begin{aligned} r_m^{n+1} = {} & \mathrm{PI}\left(\frac{\rho\, k}{\mu}\right)_{(i,j)} \left(P_w - P_{(i,j)}\right)^{n+1} - \Delta x\, \Delta y\, \frac{(\phi\rho)^{n+1}_{(i,j)} - (\phi\rho)^n_{(i,j)}}{\Delta t} \\ & + \frac{\Delta y}{\Delta x}\, k_{(i-1/2,j)} \left(\frac{\rho}{\mu}\right)_{(i-1,j)} \left(P_{(i-1,j)} - P_{(i,j)}\right)^{n+1} + \frac{\Delta y}{\Delta x}\, k_{(i+1/2,j)} \left(\frac{\rho}{\mu}\right)_{(i,j)} \left(P_{(i+1,j)} - P_{(i,j)}\right)^{n+1} \\ & + \frac{\Delta x}{\Delta y}\, k_{(i,j-1/2)} \left(\frac{\rho}{\mu}\right)_{(i,j-1)} \left(P_{(i,j-1)} - P_{(i,j)}\right)^{n+1} + \frac{\Delta x}{\Delta y}\, k_{(i,j+1/2)} \left(\frac{\rho}{\mu}\right)_{(i,j)} \left(P_{(i,j+1)} - P_{(i,j)}\right)^{n+1} \ . \end{aligned} \tag{3.4}$$

3.1.2. Energy Balance of the Fluid Body

Fluid energy balance in equation (2.5) can be rewritten in discrete form. Integration over control volume reads

$$\int \frac{\left(\phi\rho C_p T\right)^{n+1} - \left(\phi\rho C_p T\right)^n}{\Delta t} d\Omega - \int \nabla \cdot \left(\rho h \lambda \nabla P\right)^{n+1} d\Omega = \int \rho h q^w d\Omega + \int Q_h^{fr} d\Omega, \tag{3.5}$$

where the second term on LHS indicates net energy flow over control volume carried by flowing fluid. Applying Gauss divergence theorem on divergence term and substituting back into equation (3.5) the following equation is expressed

$$\int \frac{\left(\phi\rho C_p T\right)^{n+1} - \left(\phi\rho C_p T\right)^n}{\Delta t} d\Omega - \oint n \cdot \left(\rho h \lambda \nabla P\right)^{n+1} d\Gamma = \int \rho h q^w d\Omega + \int Q_h^{fr} d\Omega, \tag{3.6}$$

Equation (3.6) is not in linear form due to porosity and density dependency on pressure. In residual form, equation (3.6) reads

$$r_f^{n+1} = \int \rho h q^w d\Omega - \int \frac{\left(\phi\rho C_p T\right)^{n+1} - \left(\phi\rho C_p T\right)^n}{\Delta t} d\Omega + \oint n \cdot \left(\rho h \lambda \nabla P\right)^{n+1} d\Gamma + \int Q_h^{fr} d\Omega, \tag{3.7}$$

which indicates energy in fluid body is conserved if r_f^{n+1} is equal to zero. In discrete form, equation (3.7) is equivalent to

$$\begin{aligned} r_f^{n+1} = {} & \mathrm{PI}\left(\frac{\rho\, h\, k}{\mu}\right)_{(i,j)} \left(P_w - P_{(i,j)}\right)^{n+1} - \Delta x\, \Delta y\, \frac{\left(\phi\rho C_p T\right)^{n+1}_{(i,j)} - \left(\phi\rho C_p T\right)^n_{(i,j)}}{\Delta t} \\ & + \frac{\Delta y}{\Delta x}\, k_{(i-1/2,j)} \left(\frac{\rho\, h}{\mu}\right)_{(i-1,j)} \left(P_{(i-1,j)} - P_{(i,j)}\right)^{n+1} + \frac{\Delta y}{\Delta x}\, k_{(i+1/2,j)} \left(\frac{\rho\, h}{\mu}\right)_{(i,j)} \left(P_{(i+1,j)} - P_{(i,j)}\right)^{n+1} \\ & + \frac{\Delta x}{\Delta y}\, k_{(i,j-1/2)} \left(\frac{\rho\, h}{\mu}\right)_{(i,j-1)} \left(P_{(i,j-1)} - P_{(i,j)}\right)^{n+1} + \frac{\Delta x}{\Delta y}\, k_{(i,j+1/2)} \left(\frac{\rho\, h}{\mu}\right)_{(i,j)} \left(P_{(i,j+1)} - P_{(i,j)}\right)^{n+1} \\ & + \Delta x\, \Delta y\, AU \left(\overline{T}_{(i,j)} - T_{(i,j)}\right)^{n+1} \ . \end{aligned} \tag{3.8}$$

3.1.3. Energy Balance of the Rock Body

The third equation is energy balance in rock body from (2.8). By applying integration over volume on discrete form, the mentioned equation reads

$$\int \frac{\left((1-\phi)\,\overline{\rho}\overline{C}_p\, \overline{T}\right)^{n+1} - \left((1-\phi)\,\overline{\rho}\overline{C}_p\, \overline{T}\right)^n}{\Delta t} d\Omega - \int \nabla \cdot \left(k_r \nabla \overline{T}\right)^{n+1} d\Omega = \int Q_h^{rf} d\Omega, \tag{3.9}$$

where the second term on LHS indicates net energy flow over control volume by means of conduction in solid or rock body. Gauss divergence theorem is applied on divergence term and substituting it back into equation (3.9) reads

$$\int \frac{\left((1-\phi)\,\overline{\rho}\overline{C}_p\, \overline{T}\right)^{n+1} - \left((1-\phi)\,\overline{\rho}\overline{C}_p\, \overline{T}\right)^n}{\Delta t} d\Omega - \oint n \cdot \left(k_r \nabla \overline{T}\right)^{n+1} d\Gamma = \int Q_h^{rf} d\Omega. \tag{3.10}$$

Rearranging equation (3.10) into residual form, the above equation is written as

$$r_r^{n+1} = -\int \frac{\left((1-\phi)\overline{\rho}\overline{C}_p\,\overline{T}\right)^{n+1} - \left((1-\phi)\overline{\rho}\overline{C}_p\,\overline{T}\right)^{n}}{\Delta t}\, d\Omega + \oint n\cdot\left(k_r \nabla \overline{T}\right)^{n+1} d\Gamma + \int Q_h^{rf}\, d\Omega, \tag{3.11}$$

which indicates energy in fluid body is conserved if r_r^{n+1} is equal to zero. In discrete form, equation (3.11) can be written as

$$\begin{aligned} r_r^{n+1} = {}& \Delta x\,\Delta y\,\frac{\left((1-\phi)\overline{\rho}\overline{C}_p\,\overline{T}\right)^{n+1}_{(i,j)} - \left((1-\phi)\overline{\rho}\overline{C}_p\,\overline{T}\right)^{n}_{(i,j)}}{\Delta t} + \frac{\Delta y}{\Delta x}\,k_{r\,(i-1/2,j)}\left(\overline{T}_{(i-1,j)} - \overline{T}_{(i,j)}\right)^{n+1} \\ & + \frac{\Delta y}{\Delta x}\,k_{r\,(i+1/2,j)}\left(\overline{T}_{(i+1,j)} - \overline{T}_{(i,j)}\right)^{n+1} + \frac{\Delta x}{\Delta y}\,k_{r\,(i,j-1/2)}\left(\overline{T}_{(i,j-1)} - \overline{T}_{(i,j)}\right)^{n+1} \\ & + \frac{\Delta x}{\Delta y}\,k_{r\,(i,j+1/2)}\left(\overline{T}_{(i,j+1)} - \overline{T}_{(i,j)}\right)^{n+1} - \Delta x\,\Delta y\,AU\left(\overline{T}_{(i,j)} - T_{(i,j)}\right)^{n+1} \end{aligned} \tag{3.12}$$

3.2. Solution Strategy

As the discrete forms given in equation (3.4), (3.8), and (3.12) have non-linear dependency on primary unknown variables, one needs to perform Newton-Raphson linearisation and find the solution in iterative manner. Mathematically, it reads

$$r_e^{n+1} \approx r_e^{\nu+1} = r_e^{\nu} + J_{eP}\left(P^{\nu+1} - P^{\nu}\right) + J_{eT}\left(T^{\nu+1} - T^{\nu}\right) + J_{e\overline{T}}\left(\overline{T}^{\nu+1} - \overline{T}^{\nu}\right)\ . \tag{3.13}$$

where superscript ν and $\nu+1$ denote current and next iteration step, respectively. Note that fully implicit method (FIM) is employed to overcome strong coupling among each unknown variables. For each iteration, the fully-implicit linear system reads

$$\underbrace{\begin{bmatrix} J_{mP} & J_{mT} & J_{m\overline{T}} \\ J_{fP} & J_{fT} & J_{f\overline{T}} \\ J_{rP} & J_{rT} & J_{r\overline{T}} \end{bmatrix}}_{\mathbf{J_0}^{\nu}} \underbrace{\begin{bmatrix} \delta P \\ \delta T \\ \delta \overline{T} \end{bmatrix}}_{\delta X_0^{\nu+1}} = - \underbrace{\begin{bmatrix} r_m \\ r_f \\ r_r \end{bmatrix}}_{r_0^{\nu}} . \tag{3.14}$$

Matrix $\mathbf{J_0}^{\nu}$ in equation (3.14) is the Jacobian matrix containing all derivatives at certain iteration ν with respect to the unknown α so that each block of Jacobian matrix reads $J_{e_\alpha} = \partial r_e / \partial \alpha$. Subscripts $m, f,$ and r indicate derivatives of mass balance, fluid energy balance, and solid energy balance respectively. Note that block $J_{m\overline{T}}$ contains zero matrix since no properties in mass balance equation changes with rock temperature $\overline{T}$.

Vector $\delta X_0^{\nu+1}$ contains solutions of the linear system at fine-scale resolution. Here $\delta X^{\nu+1}$ is defined as the difference between current iteration guess and the next one so that $\delta X_0^{\nu+1} = X_0^{\nu+1} - X_0^{\nu}$. The iteration is repeated until $\delta X_0^{\nu+1} \approx 0$ or until desired convergence criterion is achieved.

The last term of equation (3.14) is residual vector r_0^{ν} which contains information of how much the conservation equation deviates. Physically, mass and energy is conserved when $r_0^{\nu} \approx 0$ or when non-linear iteration reaches convergence.

Non-linearity arising from strong coupling between three equations often leads to difficulty in achieving convergence particularly when large time step is applied. One strategy to tackle this issue is by solving the pressure block of the Jacobian first to find better initial guess for the next iteration. Physically, this strategy means a fluid flow is introduced into the system. Mathematically, it reads

$$J_{mP}\,\delta P = -r_m \tag{3.15}$$

A new linear system is constructed based on new initial pressure guess. Note that finding better pressure guess is performed only on the first iteration of the first time step, and is known as Constrained Pressure Residual (CPR) method, developed by J. Wallis [41] and later extended by several researchers [17, 42–44].

$$\underbrace{\begin{bmatrix} \widehat{J}_{mP} & \widehat{J}_{mT} & \widehat{J}_{m\overline{T}} \\ \widehat{J}_{fP} & \widehat{J}_{fT} & \widehat{J}_{f\overline{T}} \\ \widehat{J}_{rP} & \widehat{J}_{rT} & \widehat{J}_{r\overline{T}} \end{bmatrix}}_{\widehat{\mathbf{J}}_{\mathbf{0}}^{\nu}} \underbrace{\begin{bmatrix} \delta P \\ \delta T \\ \delta \overline{T} \end{bmatrix}}_{\delta X_0^{\nu+1}} = - \underbrace{\begin{bmatrix} \widehat{r}_m \\ \widehat{r}_f \\ \widehat{r}_r \end{bmatrix}}_{\widehat{r}_0^{\nu}} . \tag{3.16}$$

Here, upper tilde line ($\widehat{\ }$) indicates updated linear system with new initial pressure guess. Again, since mass balance in fluid flow has no dependency on rock temperature, the expression $\widehat{J}_{m_{\overline{T}}} = 0$ holds.

The algorithm of fully implicit geothermal reservoir simulator is shown in figure 3.2 below. Note that ϵ is user input convergence tolerance.

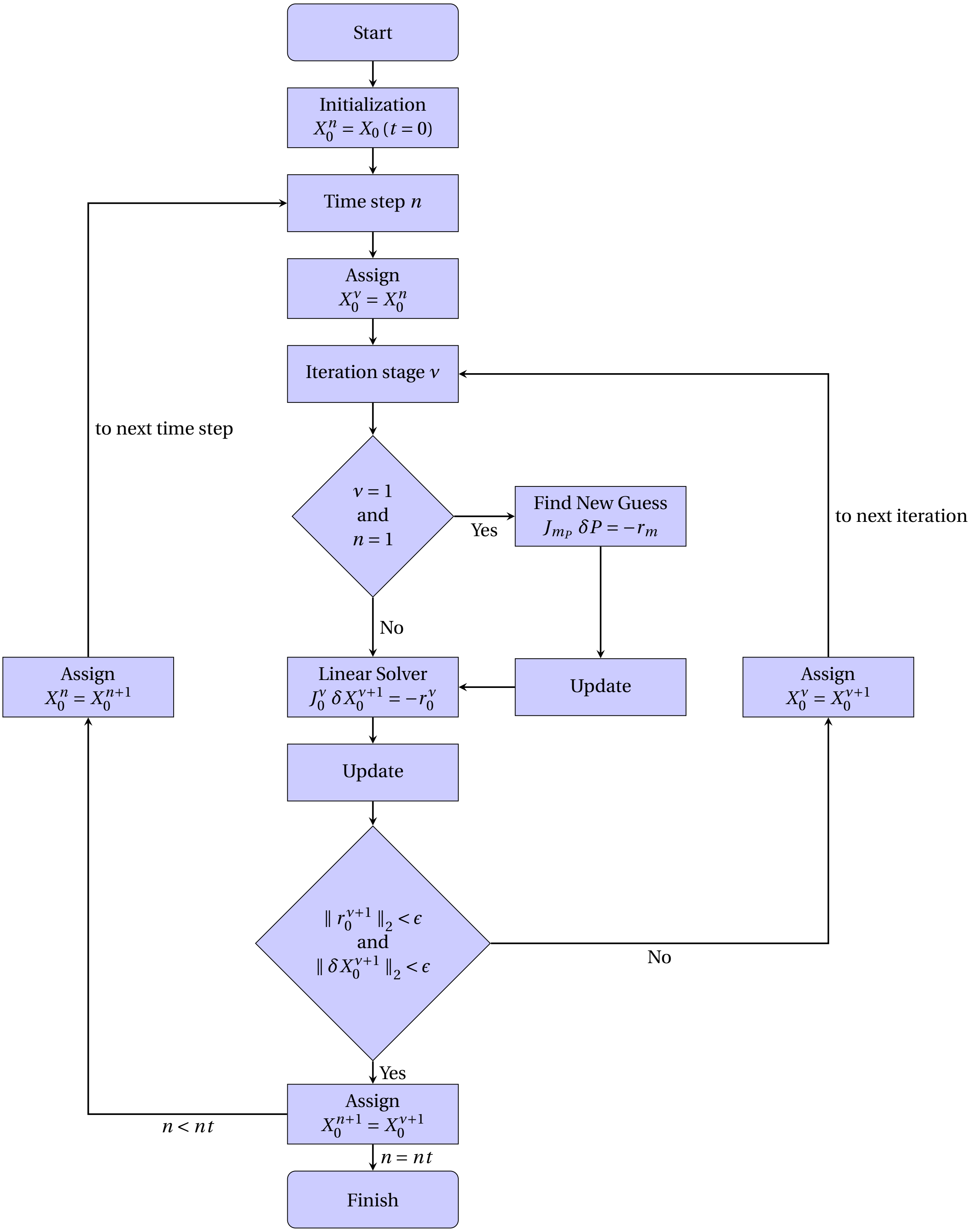
Start
Initialization
$X_0^n = X_0\,(t=0)$
Time step n
Assign
$X_0^\nu = X_0^n$
Iteration stage ν
to next time step
$\nu = 1$
and
$n = 1$
Yes
Find New Guess
$J_{mp}\,\delta P = -r_m$
to next iteration
No
Assign
$X_0^n = X_0^{n+1}$
Linear Solver
$J_0^\nu\,\delta X_0^{\nu+1} = -r_0^\nu$
Update
Assign
$X_0^\nu = X_0^{\nu+1}$
Update
$\| r_0^{\nu+1} \|_2 < \epsilon$
and
$\| \delta X_0^{\nu+1} \|_2 < \epsilon$
No
Yes
Assign
$X_0^{n+1} = X_0^{\nu+1}$
$n < nt$
$n = nt$
Finish

Figure 3.2: Flowchart of fully implicit geothermal reservoir simulator in fine-scale resolution. Subscript 0 indicates fine-scale resolution

4

Algebraic Dynamic Multilevel (ADM)

Linear system as presented in equation (3.16) provides a fully-resolved solution in fine-scale resolution. Nevertheless, in field-scale simulation, solving such linear system with high degree of freedom requires high computational cost.

One option to overcome challenges involved in computational complexity is upscaling, which aims to reduce problem size by means of finding representative average value for each reduced-size problem. However, such averaging method often costs accuracy thus consequently loses information, especially when dealing with heterogeneous reservoir.

Multiscale method, instead, constructs and solves coarse-scale systems but provides approximation of the solution at the original fine-scale resolution. This is achieved by introducing local basis functions. The map between fine-scale and coarse-scale is developed by a restriction operator, while the map of the solution from coarse back into fine-scale resolution is achieved by prolongation operator. Prolongation operator is a matrix which clusters all basis functions in its columns. This chapter discusses about construction of multiscale operators, consisting of prolongation and restriction, along with its implementation.

4.1. MSFV Operator Builder

Multiscale finite volume (MSFV) grids consists of overlapping coarse grids, namely dual and primal coarse grids in which dual coarse grid is surrounded by multiple coarse nodes at each boundary whereas primal coarse grid contains one coarse node at its center. Figure 4.1 shows an example of dual and primal coarse grids in orange and green shaded area respectively. Note that for simplicity, the multiscale framework is described in 2D domain, although 3D implementation is also possible. The global domain is divided into n_c numbers of primal coarse grid (control volume), Ω_i^c ($i \in \{1,\ldots,n_c\}$), and n_d numbers of dual coarse grid (local domain), Ω_i^d ($i \in \{1,\ldots,n_d\}$) [23, 28, 45].

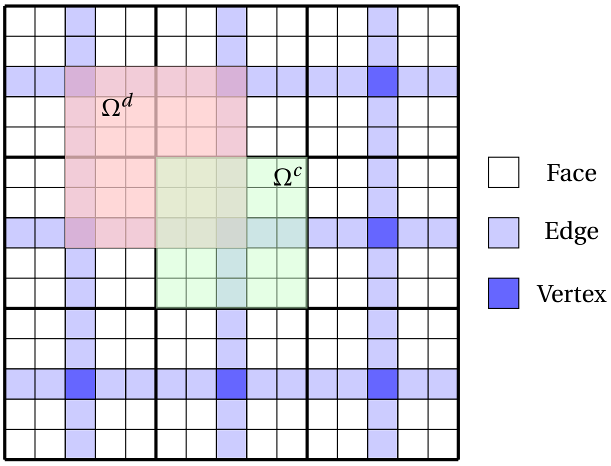

Figure 4.1: Example of 2D multiscale grids consists of 15 × 15 fine-scale resolution.

Employing MSFV to solve field-scale problem involves building of restriction and prolongation operators to reduce the size of the problem and then translate back into fine-scale resolution. Note that since pressure, fluid, and rock temperature share the same grid structure, and as to preserve conservative solution for each level, restriction operator is constructed based on finite volume (FV) method. Therefore, $\mathbf{R_m} = \mathbf{R_f} = \mathbf{R_r}$ holds, where subscript $m, f,$ and r refer to restriction operator belonging to pressure, fluid temperature, and rock temperature respectively.

FV-based restriction operator is defined as integration over control volume in which all fine grid cells j, Ω_{l-1}^{j} are summed up if they belong to primal coarse grid i, Ω_{l}^{i}. Thus, mathematically, the entry (i,j) for $\mathbf{R_m}$ between finer level $l-1$ and coarser level l reads

$$(\mathbf{R_m})_{l}^{l-1}(i,j) = \begin{cases} 1, & \text{if } \Omega_{l-1}^{j} \subset \Omega_{l}^{i} \\ 0, & \text{otherwise} \end{cases}, \quad \forall_{i} \in \{1,\ldots,n_l\};\ \forall_{j} \in \{1,\ldots,n_{l-1}\}. \tag{4.1}$$

Pressure and rock temperature as presented in equation (2.2) and (2.8), respectively, show parabolic nature, whilst fluid temperature in equation (2.5) has hyperbolic nature. One may consider different prolongation operators for parabolic and hyperbolic quantities.

Multiscale prolongation is suitable for parabolic problem in which the basis function is a set of local solution in dual coarse grids. As such, elliptic part is required for basis function construction. Note that solving elliptic part captures fine-scale heterogeneity. Basis functions between two consecutive levels are algebraically constructed as described in [28, 45].

Fine-scale pressure solution is approximated by multiplication of prolongation operator and coarse-scale pressure solution. Algebraically, this reads

$$P \approx P' = \mathbf{P_m} \times P^{c}, \tag{4.2}$$

where P^{c} is pressure at coarse nodes, and $\mathbf{P_m}$ is pressure prolongation which is constructed from basis functions Φ_k for each column as follows

$$\mathbf{P_m} = \begin{bmatrix} \vdots & \vdots & \cdots & \vdots & \vdots \\ \Phi_1 & \Phi_2 & \cdots & \Phi_{n_c-1} & \Phi_{n_c} \\ \vdots & \vdots & \cdots & \vdots & \vdots \end{bmatrix}_{n \times n_c}. \tag{4.3}$$

Similarly, with the same algebraic procedure, fine-scale rock temperature solution is approximated by multiplication of prolongation operator and coarse-scale rock temperature solution. Algebraically, this reads

$$\overline{T} \approx \overline{T}' = \mathbf{P_r} \times \overline{T}^{c}, \tag{4.4}$$

where $\overline{T}^{c}$ is rock temperature at coarse nodes, and $\mathbf{P_r}$ is rock temperature prolongation. Similar to construction of pressure prolongation in equation (4.3), rock temperature prolongation consist of ψ_k for each column and reads

$$\mathbf{P_r} = \begin{bmatrix} \vdots & \vdots & \cdots & \vdots & \vdots \\ \psi_1 & \psi_2 & \cdots & \psi_{n_c-1} & \psi_{n_c} \\ \vdots & \vdots & \cdots & \vdots & \vdots \end{bmatrix}_{n \times n_c}. \tag{4.5}$$

Unlike pressure and rock temperature, fluid temperature is a hyperbolic variable. Constant prolongation is considered for fluid temperature which means prolongation is constructed as transpose of corresponding restriction operator. Mathematically, it reads

$$(\mathbf{P_f}) = (\mathbf{R_f})^{\mathbf{T}}. \tag{4.6}$$

4.2. ADM Solution Strategy

ADM method provides solution of fully-resolved fine-scale discrete system as presented in equation (3.16) on dynamic multilevel grid. Consider the domain consists of $N_0 = N_0^x \times N_0^y$ number of fine cells (in 3D N_0^z is also considered). Hierarchically nested coarse grids are employed in which the grids are coarsened at each coarsening level l with certain coarsening ratio γ_l, such that

$$\gamma_l = \left(\gamma_l^x, \gamma_l^y\right) = \left(\frac{N_{l-1}^x}{N_l^x}, \frac{N_{l-1}^y}{N_l^y}\right), \tag{4.7}$$

holds (in 3D γ_l^z is also considered). Recall fine-scale linear system in equation (3.16) and combine with sequence of restriction and prolongation operators to construct ADM linear system. Linear system in ADM scale reads

$$\underbrace{\mathbf{R}_l^{l-1} \cdots \mathbf{R}_1^0 \; \widehat{\mathbf{J}}_\mathbf{0}^\nu \; \mathbf{P}_0^1 \cdots \mathbf{P}_{l-1}^l}_{J_{ADM}} \; \delta X_l^{\nu+1} = -\underbrace{\mathbf{R}_l^{l-1} \cdots \mathbf{R}_1^0 \; \widehat{r}_0^\nu}_{r_{ADM}}, \tag{4.8}$$

where $\delta X_l^{\nu+1}$ refers to ADM solution.

Once the solution is obtained in ADM resolution, fine-scale solution is approximated through a sequence of prolongation operators from ADM solution. Therefore, fine-scale approximation reads

$$\delta X_0 \approx \delta X_0' = \mathbf{P}_0^1 \cdots \mathbf{P}_{l-1}^l \, \delta X_l \,. \tag{4.9}$$

Static prolongation operators $\mathbf{P}_{l-1}^l$ in equation (4.9) are constructed from block diagonal structure of three sub-prolongations as the following

$$\mathbf{P}_{l-1}^l = \begin{bmatrix} (\mathbf{P_m})_{l-1}^l & 0 & 0 \\ 0 & (\mathbf{P_f})_{l-1}^l & 0 \\ 0 & 0 & (\mathbf{P_r})_{l-1}^l \end{bmatrix}_{N_{l-1} \times N_l} . \tag{4.10}$$

Similarly, block structure of restriction operator $\mathbf{R}_l^{l-1}$ consist of three block diagonal sub-restriction matrix of the form

$$\mathbf{R}_l^{l-1} = \begin{bmatrix} (\mathbf{R_m})_l^{l-1} & 0 & 0 \\ 0 & (\mathbf{R_f})_l^{l-1} & 0 \\ 0 & 0 & (\mathbf{R_r})_l^{l-1} \end{bmatrix}_{N_l \times N_{l-1}} . \tag{4.11}$$

4.3. Selection of ADM Grid

Note that although static prolongation and restriction operators are built in entire domain, only some fractions of the domain need to be coarsened. For instance, one may need to keep the region near temperature front, geological features with high contrasts and wells in fine-scale resolution [1].

At each time step n, ADM grids are dynamically selected based on grid selection criterion. Consider a set of coarse cells Ω_l^c neighboring with fine grid cells Ω_l^f at coarsening level l. The grid selection criterion is built in the basis of tracking fluid temperature front. Mathematically, it can be defined by relative differences of fluid temperature between both sets of cell as follows

$$\Delta T_{i,j} = \frac{\max\left(|T_i - T_j|\right)}{|T_{inj} - T_{prod}|}, \quad \forall i \in \Omega_l^c \text{ and } \forall j \in \Omega_l^f, \tag{4.12}$$

where T_{inj} and T_{prod} are injector well and producer well temperatures respectively. Coarse cell Ω_l^c is refined into similar resolution to fine cells Ω_l^f if the condition

$$\Delta T_{i,j} > \delta_T, \tag{4.13}$$

is satisfied. Here, δ_T is a user-defined ADM tolerance. Equation (4.13) physically means grid refinement is only performed when significant fluid temperature change is observed. Thus, allowing one to capture fluid temperature front in fine-scale resolution. In addition, on the area close to wells, fine-scale resolution is employed to ensure that well fluxes are captured accurately. Note that to maintain numerical accuracy, only one level transition among the neighboring cells is allowed. In other words, any grid cells at certain level l can only be surrounded by any other cells at $(l-1)$ or $(l+1)$ level. The algorithm of fully implicit geothermal reservoir simulator in ADM grid is presented in figure 4.2 below.

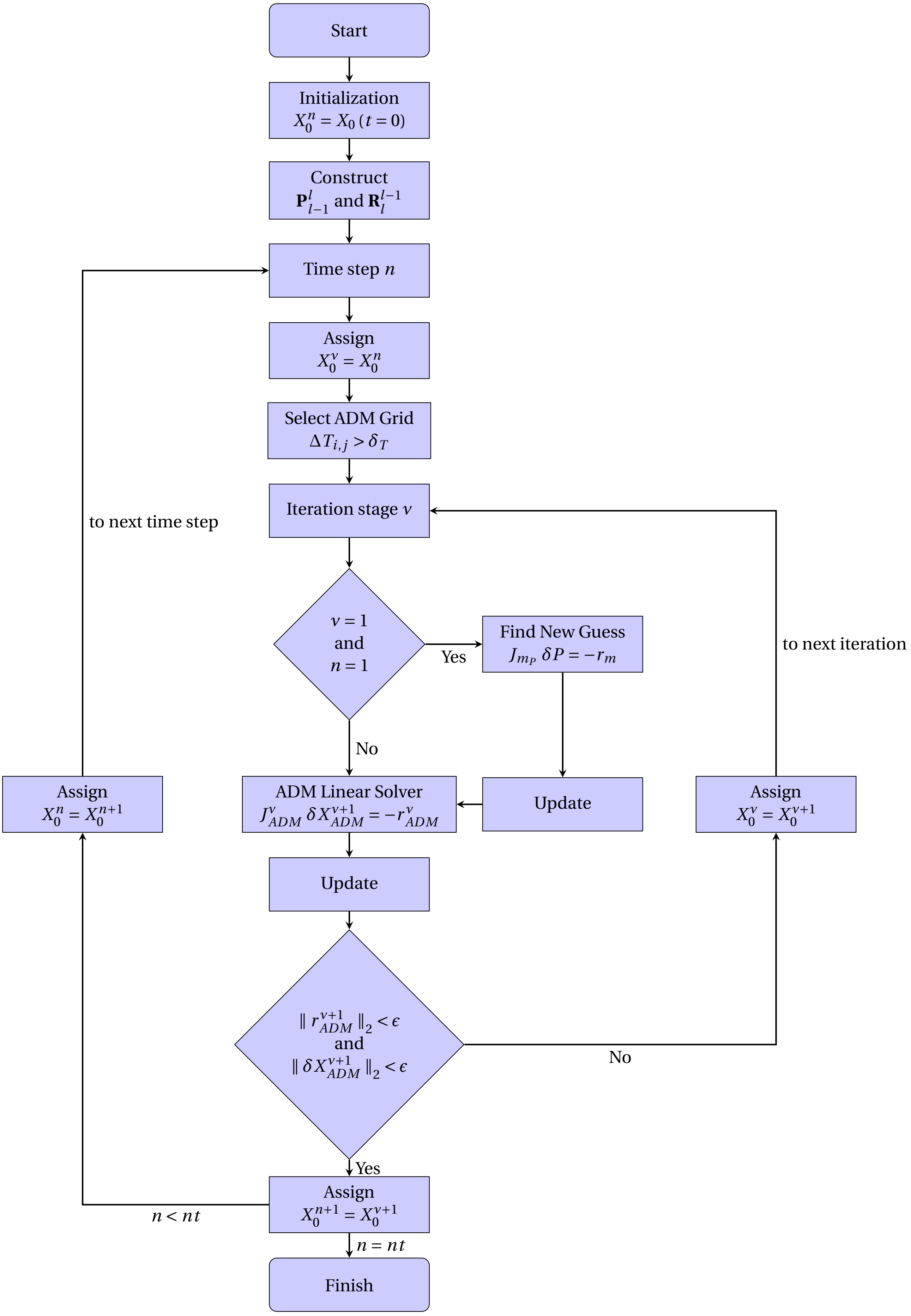
Start
Initialization
$X_0^n = X_0\,(t=0)$
Construct
$\mathbf{P}_{l-1}^{l}$ and $\mathbf{R}_{l}^{l-1}$
Time step n
Assign
$X_0^{\nu} = X_0^n$
Select ADM Grid
$\Delta T_{i,j} > \delta_T$
Iteration stage ν
to next time step
$\nu = 1$ and $n = 1$
Yes
Find New Guess
$J_{m_P}\,\delta P = -r_m$
to next iteration
No
Assign
$X_0^n = X_0^{n+1}$
ADM Linear Solver
$J_{ADM}^{\nu}\,\delta X_{ADM}^{\nu+1} = -r_{ADM}^{\nu}$
Update
Assign
$X_0^{\nu} = X_0^{\nu+1}$
Update
$\parallel r_{ADM}^{\nu+1} \parallel_2 < \epsilon$ and $\parallel \delta X_{ADM}^{\nu+1} \parallel_2 < \epsilon$
No
Yes
Assign
$X_0^{n+1} = X_0^{\nu+1}$
$n < nt$
$n = nt$
Finish

Figure 4.2: Flowchart of fully implicit geothermal reservoir simulator in ADM resolution. Note that the algorithm involves static prolongation and restriction operators.

5

Result and Discussion

In this chapter, numerical results of geothermal ADM simulation are presented. For all cases, a 2D 216 [m] ×54 [m] incompressible geothermal reservoir is considered and divided into 216 × 54 fine-scale grid blocks. The reservoir undergoes continuous injection with constant temperature 300 [K] from injector wells, whereas production temperature is assumed similar to fluid temperature at cell where the well is situated. Injector and producer wells are pressure-constrained with borehole pressure 30 [MPa] and 10 [MPa] respectively for all test cases. Note that along all boundaries, no-flow boundary condition is imposed. Furthermore, the reservoir was initialized at pressure 20 [MPa] and temperature 400 [K].

The accuracy of ADM solution is compared with fine-scale solution and percentage of active grids in ADM method compared to total number of grids in fine-scale resolution. For each time step, error of ADM method is given as

$$\varepsilon_X(t) = \frac{\parallel X_{FS}(t) - X_{ADM}(t) \parallel_2}{\parallel X_{FS}(t) \parallel_2}, \quad X \in \{P, T, \overline{T}\} \ . \tag{5.1}$$

The accuracy of ADM solution is evaluated over entire time step and calculated as

$$\varepsilon_X = mean(\varepsilon_X(t)), \quad X \in \{P, T, \overline{T}\} \ . \tag{5.2}$$

The effect of non-thermal equilibrium is evaluated in early stage of injection and calculated as absolute difference between fluid and rock temperature

$$\Delta T_{eq} = \mid T(t) - \overline{T}(t) \mid \ . \tag{5.3}$$

General input parameters for all test cases are presented in table 5.1 below.

Table 5.1: Fluid and rock properties for numerical simulation.

Properties	Symbol	Value	Unit
Fluid conductivity	k_f	0.591	$\frac{W}{m \cdot K}$
Fluid specific heat	C_p	4200	$\frac{J}{kg \cdot K}$
Rock conductivity	k_r	4	$\frac{W}{m \cdot K}$
Rock specific heat	$\overline{C}_p$	790	$\frac{J}{kg \cdot K}$
Rock density	$\overline{\rho}$	2750	$\frac{kg}{m^3}$
Matrix porosity	ϕ	0.1	$[-]$
Well productivity index	PI	1000	m
Initial pressure	P^0	20	MPa
Initial fluid temperature	T^0	400	K
Initial rock temperature	$\overline{T}^0$	400	K

5.1. Case 1 : Homogeneous Reservoir

A 2D isotropic and homogeneous reservoir with the value of matrix permeability $k = 10^{-14}$ [m^2] is considered. Quarter of five-spot injection pattern is simulated where injector and producer wells are situated on the bottom left corner and top right corner of the reservoir respectively.

Figure 5.1 shows comparison between fine-scale solution with ADM solution with 10% tolerance. Temperature front is captured by fine-scale resolution, whereas on the area away from temperature front, problem is resolved in coarser resolution. Note that fine-scale resolution is also preserved on the area near injector and producer wells. Also note that fine-scale resolution is no longer observed around temperature front in larger injection time. As shown in figure 5.2, highly diffused temperature front leads to more employment of coarser grids.

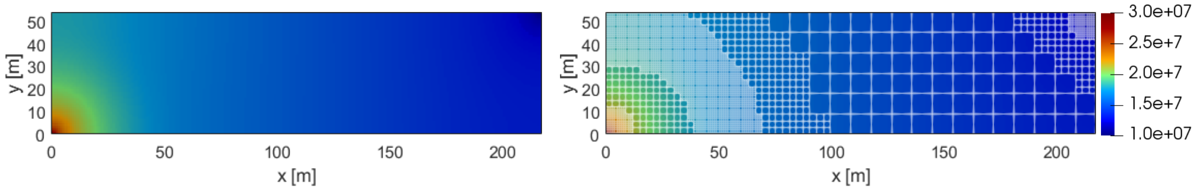

(a) Pressure [Pa]

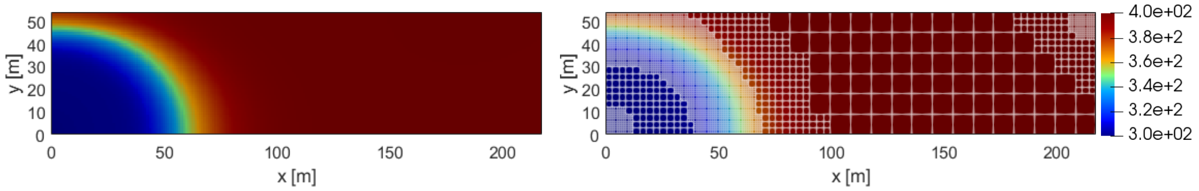

(b) Fluid Temperature [K]

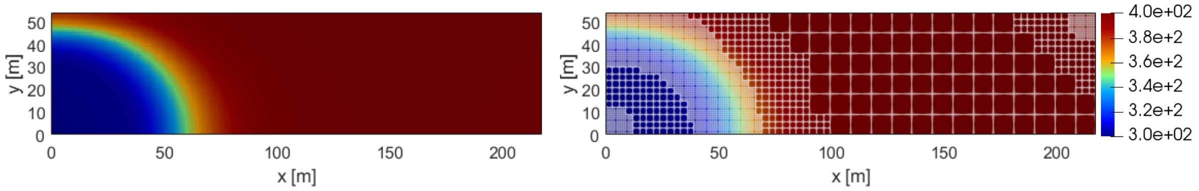

(c) Rock Temperature [K]

Figure 5.1: Solution after 250 days of injection in homogeneous reservoir. Fine-scale solution (left) is approximated by ADM solution (right) with $\delta T = 10\%$ corresponding to 17% of active grids.

Figure 5.3 (a) shows the error imposed by ADM method compared to fine-scale solution as reference corresponding to the result shown in figure 5.2. In general, error profile shows proportional relationship with ADM tolerance. On low ADM tolerance value, ADM is very sensitive to slight fluid temperature change mainly around fluid temperature front. Inversely, high ADM tolerance reduces the ability to capture fluid temperature front. As a result of low ADM tolerance, the grids are refined to fine-scale resolution and consequently greater number of active grids as illustrated in figure 5.3 (b). Figure 5.3 (c) shows history of active grids during simulation corresponding to the result in figure 5.2. The simulation is started initially with coarser grids regardless of what ADM tolerance is employed. Note that decreasing number of active grids on high ADM tolerance is associated with more steady and diffused heat flow.

Figure 5.4 shows temperature difference of fluid and rock in four different simulation time. Note that both temperatures reach equilibrium in very short time. The resulting low velocity ensures sufficient contact time between rock and fluid, thus enabling massive heat exchange over large area and time. Consequently, nearly-identical fluid and rock temperatures are observed in entire homogeneous reservoir.

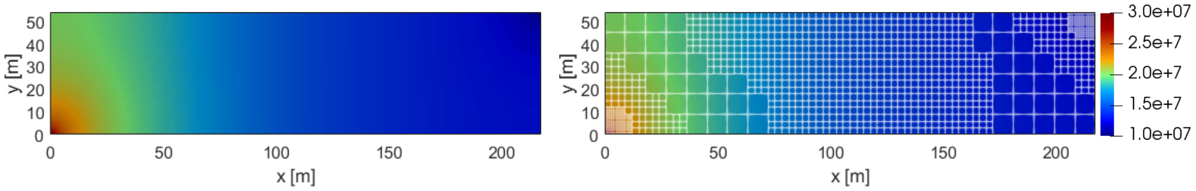

(a) Pressure [Pa]

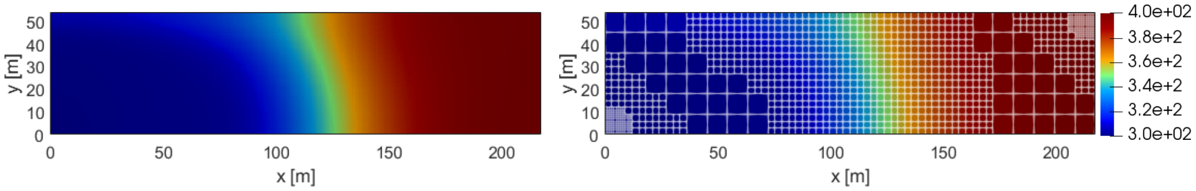

(b) Fluid Temperature [K]

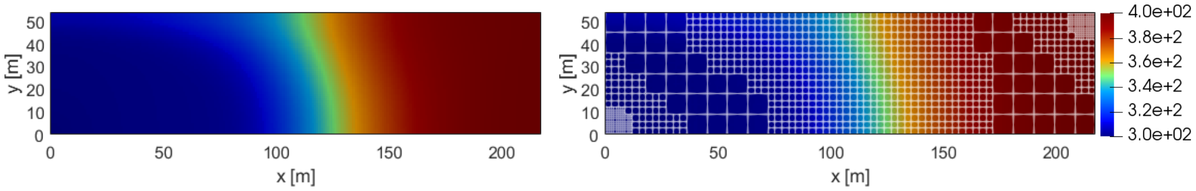

(c) Rock Temperature [K]

Figure 5.2: Solution after 750 days of injection in homogeneous reservoir. Fine-scale solution (left) is approximated by ADM solution (right) with $\delta T = 10\%$ corresponding to 17% of active grids. Note that diffused temperature front is sufficiently captured by coarser grids.

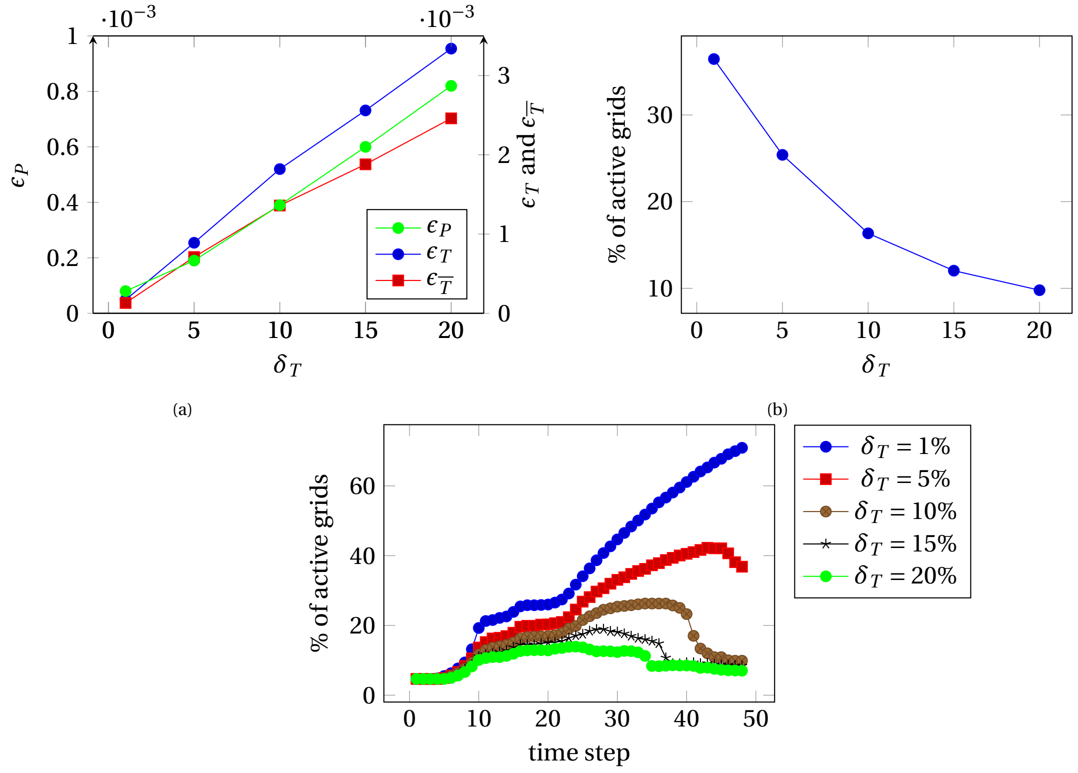

(a)

(b)

(c)

Figure 5.3: Test Case 1 : Error of ADM solution with respect to fine-scale reference (a) and percentage of ADM active grids as function of ADM tolerance (b), and history of ADM grids during simulation (c).

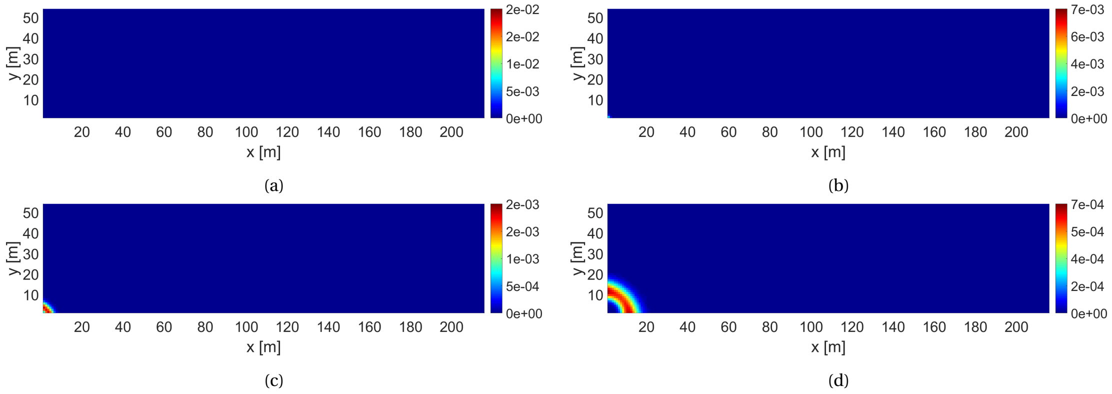

Figure 5.4: Test Case 1 : Absolute temperature difference of fluid and rock [K] after 0.01 (a), 0.1 (b), 1 (c), and 10 (d) days of injection.

5.2. Case 2 : Blocky-Homogeneous Reservoir

Case 2 aims to test ADM performance to simulate fluid flow in 2D homogeneous reservoir with 10^{-14} [m^2] permeability and 10^{-18} [m^2] permeability barrier as illustrated in figure 5.5 is considered. Two producers and one injector wells are randomly placed across the reservoir.

Figure 5.6 shows ADM solution along with fine-scale solution after 200 days of injection. Note that fine-scale grids are automatically preserved around wells and temperature front. Also note that ADM allows refinement and coarsening in higher or lower consecutive level.

Figure 5.7 shows the sensitivity of ADM solution with respect to ADM tolerance (a) and number of active grid cells for different value of ADM tolerance (b). Note that the presence of permeability barrier leads to larger temperature front area thus more active grids. Also note that the three involved wells contribute around 15% of total active grids. Figure 5.7 (c) presents history of involved grids during simulation for different ADM tolerance corresponding to the results in figure 5.6.

Figure 5.8 shows absolute temperature difference during early stage of injection in blocky-homogeneous reservoir. Note that the temperature difference is considerably negligible despite the presence of permeability barrier.

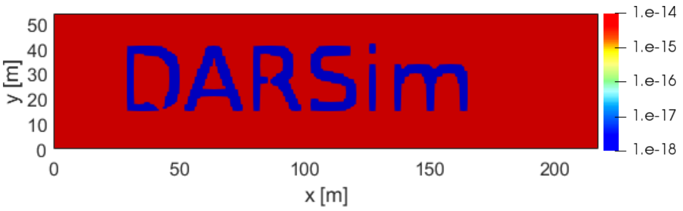

Figure 5.5: Blocky-homogeneous permeability field [m^2] used in test case 4.

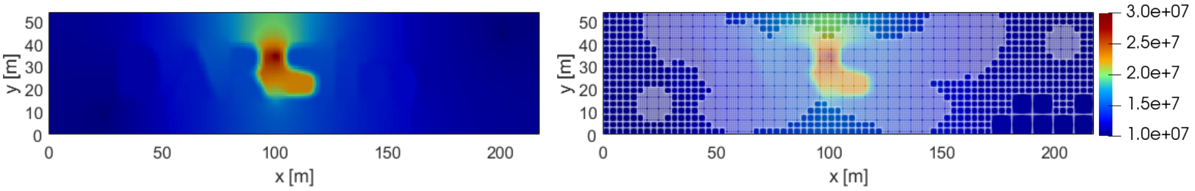

(a) Pressure [Pa]

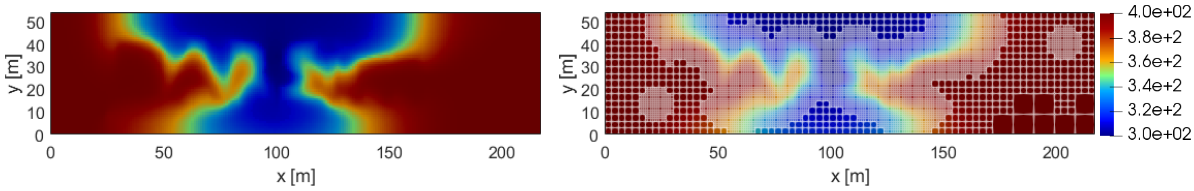

(b) Fluid Temperature [K]

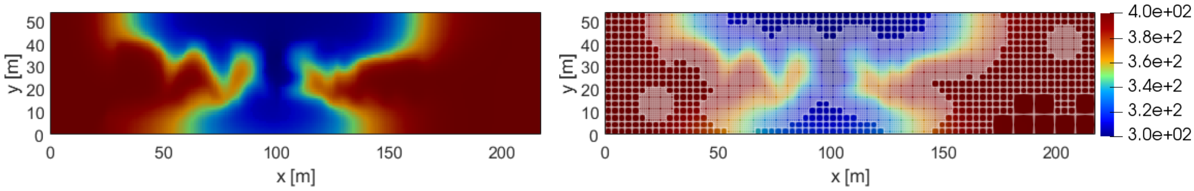

(c) Rock Temperature [K]

Figure 5.6: Solution after 200 days of injection in blocky-homogeneous reservoir. Fine-scale solution (left) is approximated by ADM solution (right) with $\delta T = 10\%$ corresponding to 35% of active grids at the end of simulation.

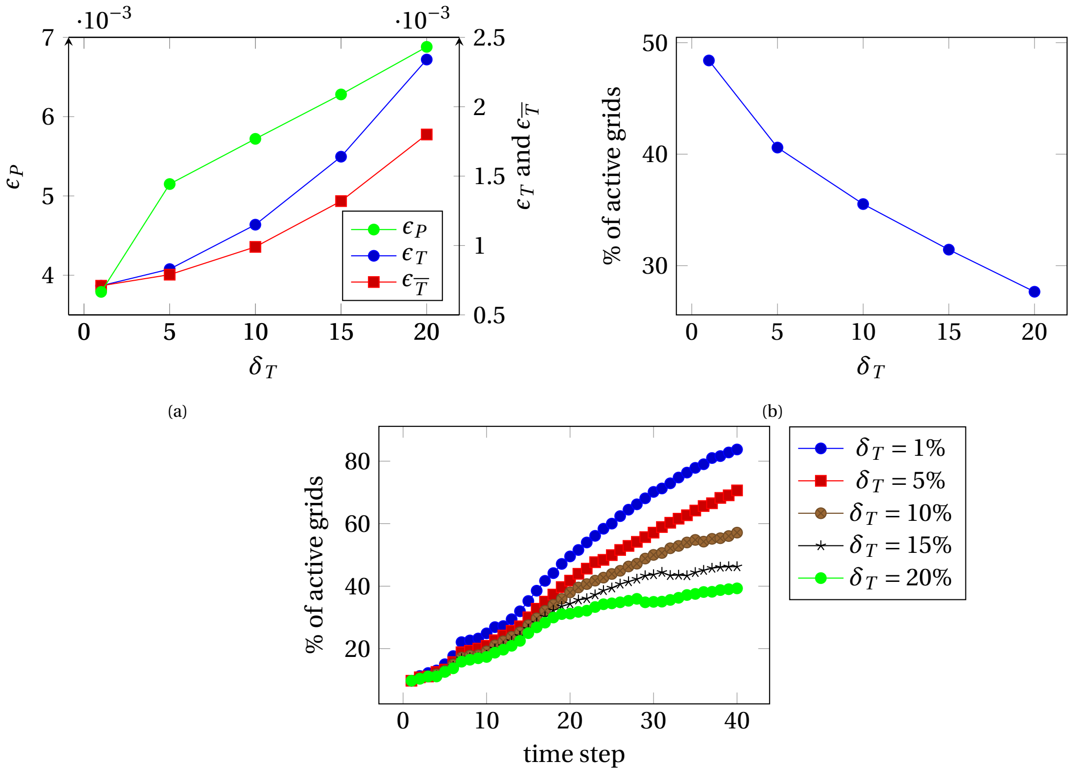

(a)

(b)

(c)

Figure 5.7: Test Case 2 : Error of ADM solution with respect to fine-scale reference (a) and percentage of ADM active grids as function of ADM tolerance (b), and history of ADM grids during simulation (c).

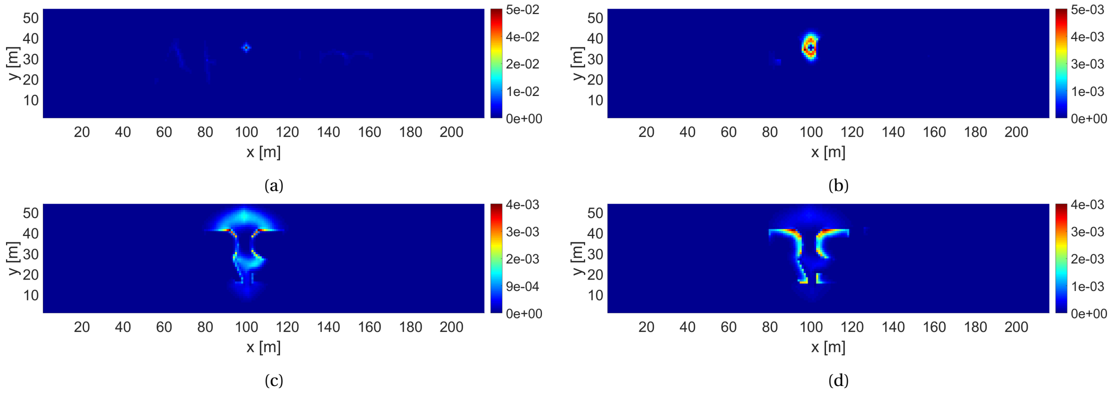

Figure 5.8: Test Case 2 : Absolute temperature difference of fluid and rock [K] after 0.01 (a), 0.1 (b), 1 (c), and 10 (d) days of injection.

5.3. Case 3 : Patchy-Heterogeneous Reservoir

Case 3 involves injection of cold water in 2D patchy-heterogeneous reservoir which is extracted from SPE10 top layer permeability database and shown in figure 5.9. Pressure-constrained producer and injector wells are situated on the bottom left corner and top right corner of the reservoir respectively.

Figure 5.10 shows ADM solution approximating fine-scale solution after 65 days of injection. As fluid energy balance has hyperbolic nature, energy is influenced by characteristic velocity of the flowing fluid as its carrier. As such, temperature front exhibits unique pattern influenced by permeability field. Additionally, steep pressure gradient is observed on the left part of the reservoir where high permeability contrast exists. Note that multiscale prolongation for pressure captures this heterogeneity and results similarly to fine-scale pressure solution.

Figure 5.11 (a) shows the sensitivity of ADM solution with respect to ADM tolerance. Note that ADM method with sequence of restriction and prolongation operators provide approximation with reasonably acceptable error. Figure 5.11 (b) shows that ADM tolerance leads to greater number of active grids during simulation thus consequently more accurate result. Figure 5.11 (c) presents history of involved grids during simulation for different ADM tolerance. Note that the number of actives grids is selected based on dynamic evolution of fluid temperature profile.

Figure 5.12 shows absolute temperature difference during early stage of injection in patchy-heterogeneous reservoir. Note that temperature difference remains unaffected by permeability contrast. Large fluid-rock contact area ensures efficient heat exchange.

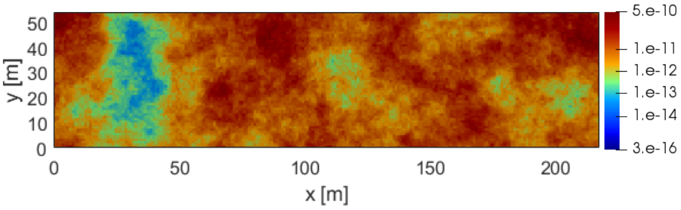

Figure 5.9: Heterogeneous permeability field [m^2] extracted from SPE10 top layer permeability database.

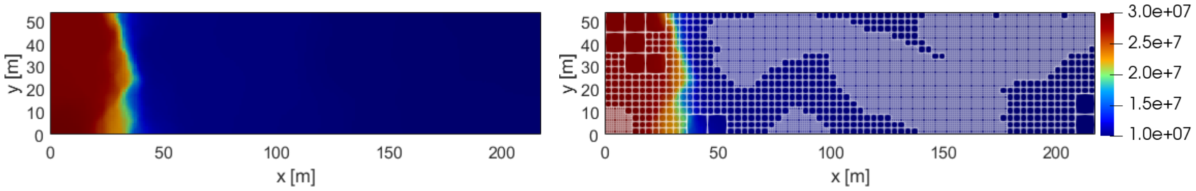

(a) Pressure [Pa]

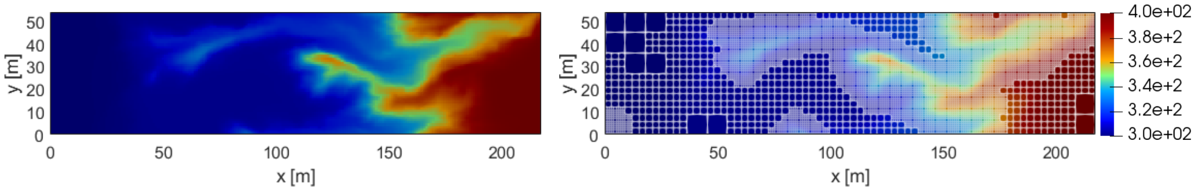

(b) Fluid Temperature [K]

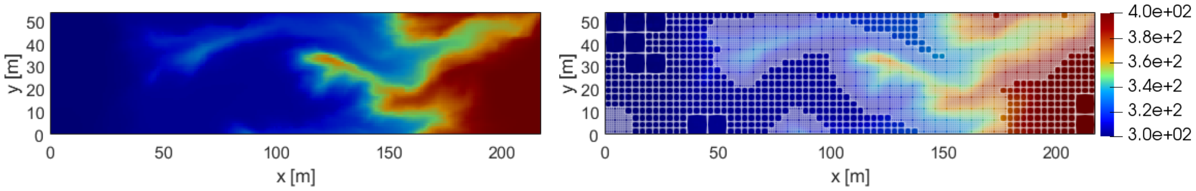

(c) Rock Temperature [K]

Figure 5.10: Solution after 65 days of injection in patchy-heterogeneous reservoir. Fine-scale solution (left) is approximated by ADM solution (right) with δT = 10% corresponding to 37% of active grids.

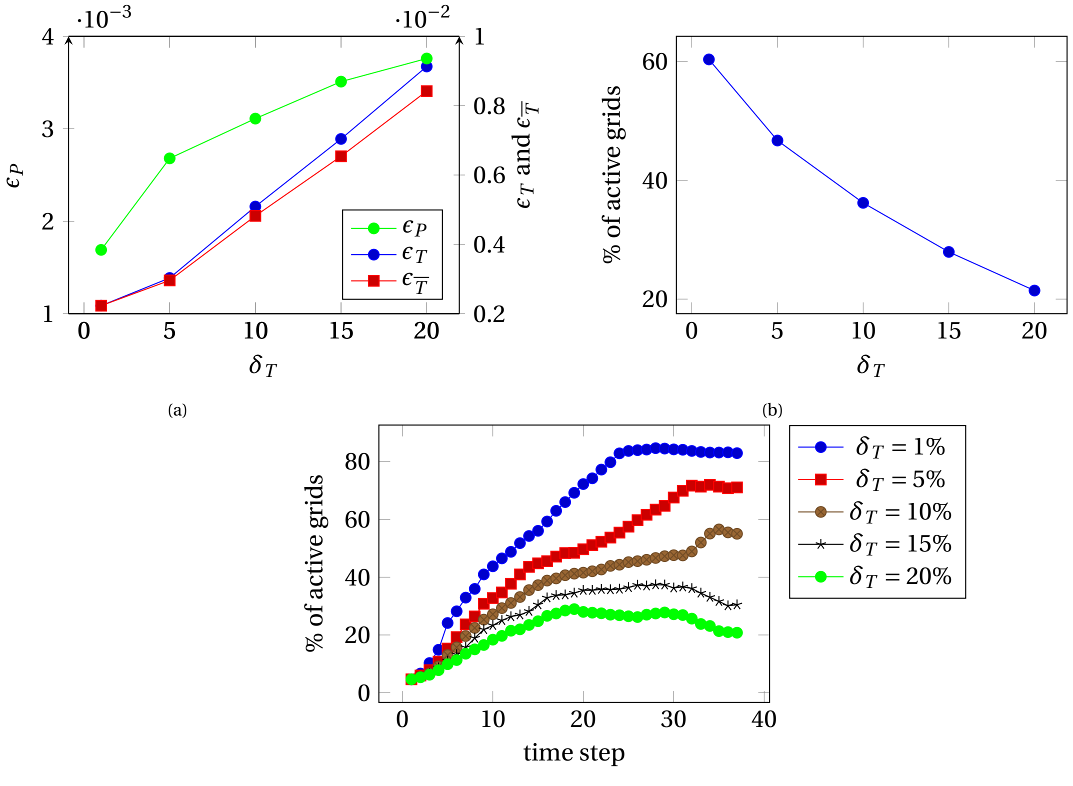

(a)

(b)

(c)

Figure 5.11: Test Case 3 : Error of ADM solution with respect to fine-scale reference (a) and percentage of ADM active grids as function of ADM tolerance (b), and history of ADM grids during simulation (c).

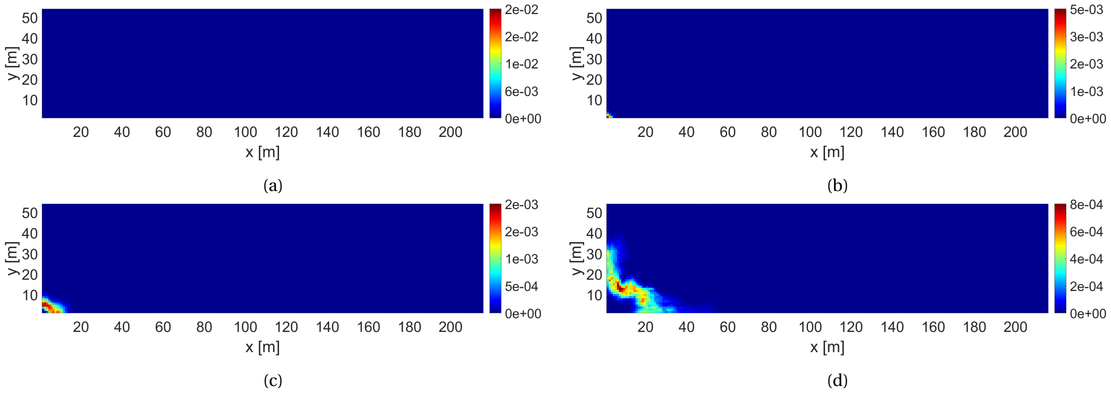

(a) (b)

(c) (d)

Figure 5.12: Test Case 3 : Absolute temperature difference of fluid and rock [K] after 0.01 (a), 0.1 (b), 1 (c), and 10 (d) days of injection.

5.4. Case 4 : Channelized-Heterogeneous Reservoir

Case 4 involves injection of cold water in 2D channelized-heterogeneous reservoir. Producer and injector well are respectively placed on top left and bottom right corner of the reservoir. As such, cold water predominantly flows through dominant high permeable channel as shown in figure 5.13. As such, the effect of high velocity fluid with regards to non-thermal equilibrium will be investigated.

Figure 5.14 presents solution after 75 days of injection. Higher velocity along the preferred paths leads to distinct temperature front. Note that larger temperature front coverage results in higher number of active grids. The effect of progressing temperature front leads to non-unified distribution fine-scale grid. Note that the resulting pressure gradient around injection well is less steep compared to test case 3. This is due to the fact that the flow is parallel to high permeable channel.

Figure 5.15 shows the sensitivity of ADM solution accuracy with respect to ADM tolerance (a) and number of active grids for different value of ADM tolerance (b). Note that compared to test case 3, the percentage of active grids increases which can be associated with steeper temperature front as the effect of higher velocity. Figure 5.15 (c) presents history of involved grids during simulation for different ADM tolerance corresponding to the results in figure 5.14. Note that fluctuation of active grids history during simulation can be associated with temperature front coverage area and breakthrough.

Figure 5.16 shows absolute temperature difference during early stage of injection in channelized and heterogeneous reservoir. Note that temperature difference remains negligible regardless of the presence of high permeable channel.

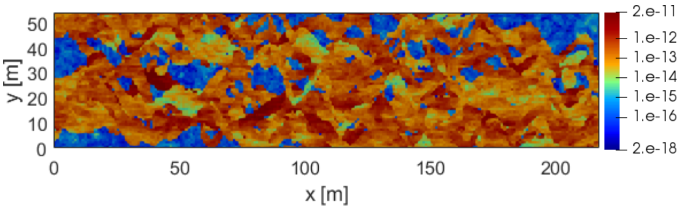

Figure 5.13: Heterogeneous permeability field [m^2] extracted from SPE10 bottom layer permeability database.

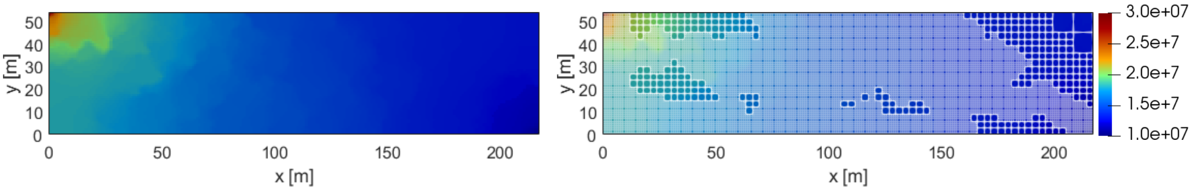

(a) Pressure [Pa]

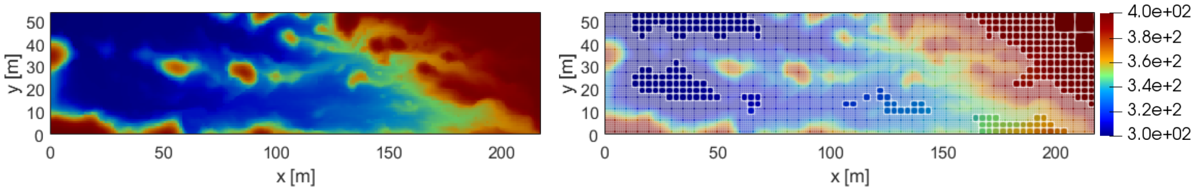

(b) Fluid Temperature [K]

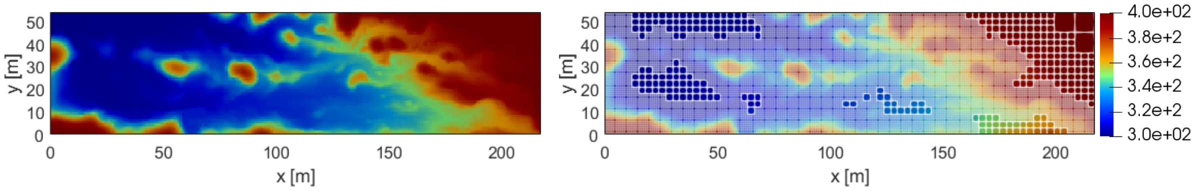

(c) Rock Temperature [K]

Figure 5.14: Solution after 75 days of injection in channelized-heterogeneous reservoir. Fine-scale solution (left) is approximated by ADM solution (right) with $\delta T = 10\%$ corresponding to 43% of active grids.

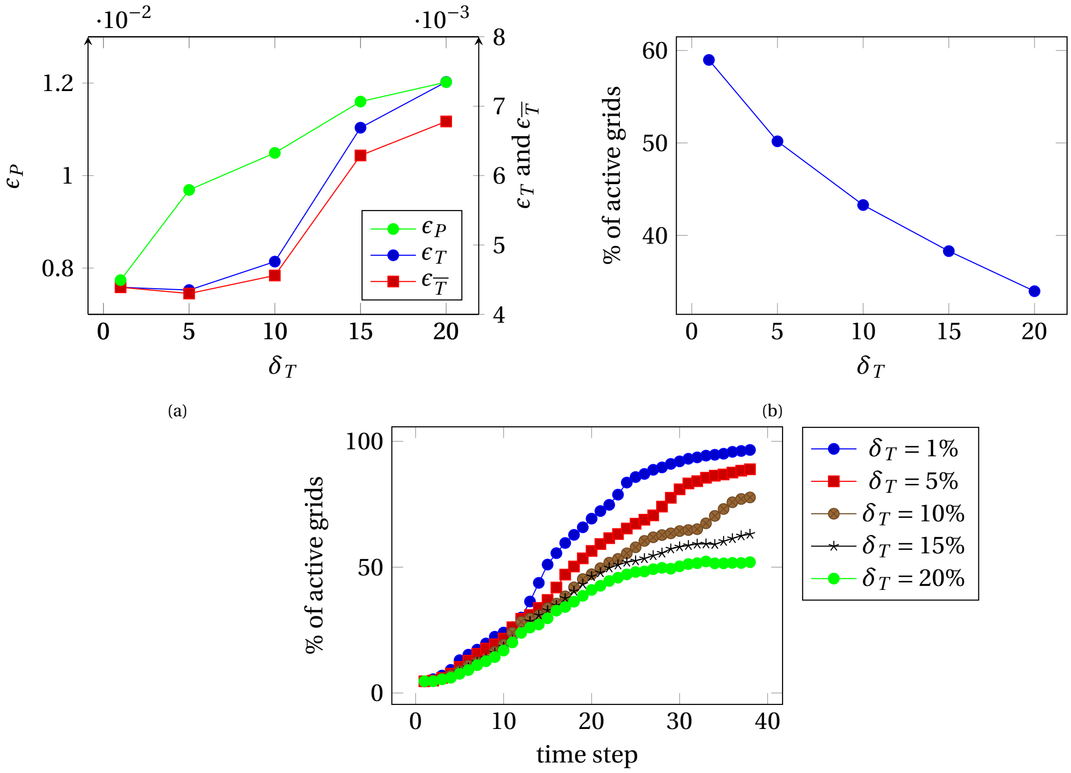

(a)

(b)

(c)

Figure 5.15: Test Case 4 : Error of ADM solution with respect to fine-scale reference (a) and percentage of ADM active grids as function of ADM tolerance (b), and history of ADM grids during simulation (c).

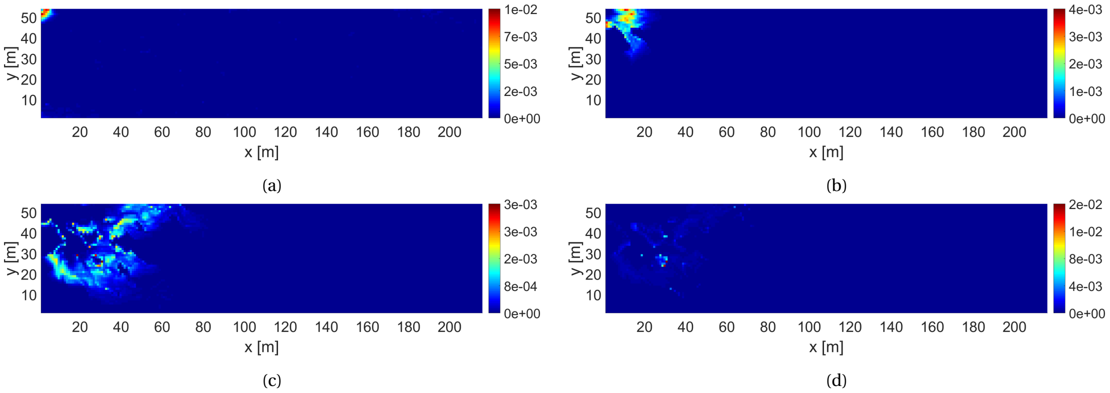

(a) (b)

(c) (d)

Figure 5.16: Test Case 4 : Absolute temperature difference of fluid and rock [K] after 0.01 (a), 0.1 (b), 1 (c), and 10 (d) days of injection.

5.5. Case 5 : Anisotropic-Heterogeneous Reservoir

Case 5 aims to test ADM performance to simulate fluid flow in a more challenging environment. A 2D heterogeneous and anisotropic reservoir is considered. Producer and one injector wells are placed on the bottom left and top right corner so that water flow to reverse direction. SPE10 top layer in figure 5.9 is set for permeability in x-direction, while permeability in y-direction follows SPE10 bottom layer in figure 5.13.

Figure 5.17 shows ADM solution along with fine-scale solution after 50 days of injection. ADM shows good agreement to fine-scale solution. Additionally, both fluid and rock temperature do not differ significantly despite flow in different velocity and direction.

Figure 5.18 shows the sensitivity of ADM solution with respect to ADM tolerance (a) and number of active grid cells for different value of ADM tolerance (b). Note that high permeability contrast leads to slightly greater error compared to other test cases. Figure 5.18 (c) presents history of involved grids during simulation for different ADM tolerance corresponding to the results in figure 5.17. Note that the least sensitive ADM tolerance shows close to 100%. This is due to many preferred flow paths in x and y direction from anisotropy.

Figure 5.19 shows absolute temperature difference during early stage of injection in anisotropic and heterogeneous reservoir. Note that temperature difference remains negligible regardless of irregular preferred flow path from anisotropic reservoir, thus verifying thermal equilibrium assumption.

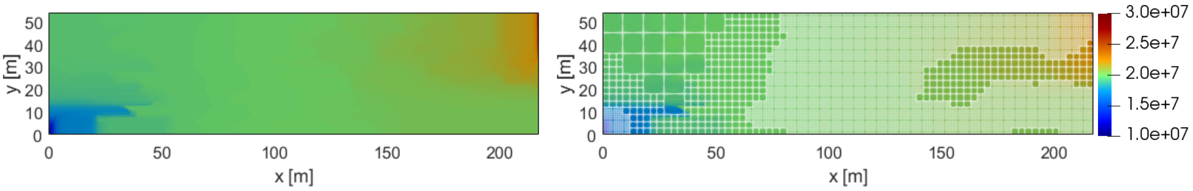

(a) Pressure [Pa]

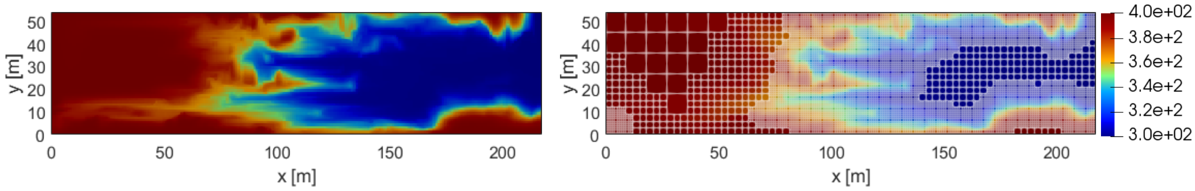

(b) Fluid Temperature [K]

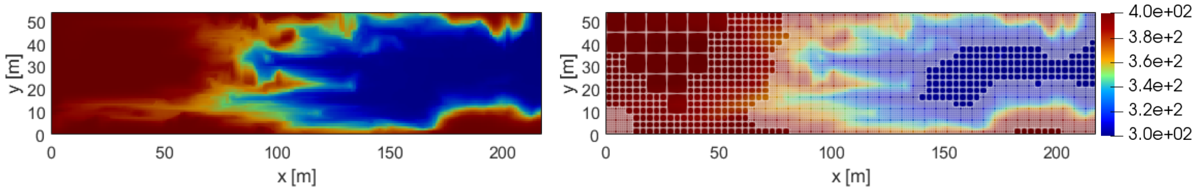

(c) Rock Temperature [K]

Figure 5.17: Solution after 50 days of injection in anisotropic-heterogeneous reservoir. Fine-scale solution (left) is approximated by ADM solution (right) with $\delta T = 13\%$ corresponding to 38% of active grids.

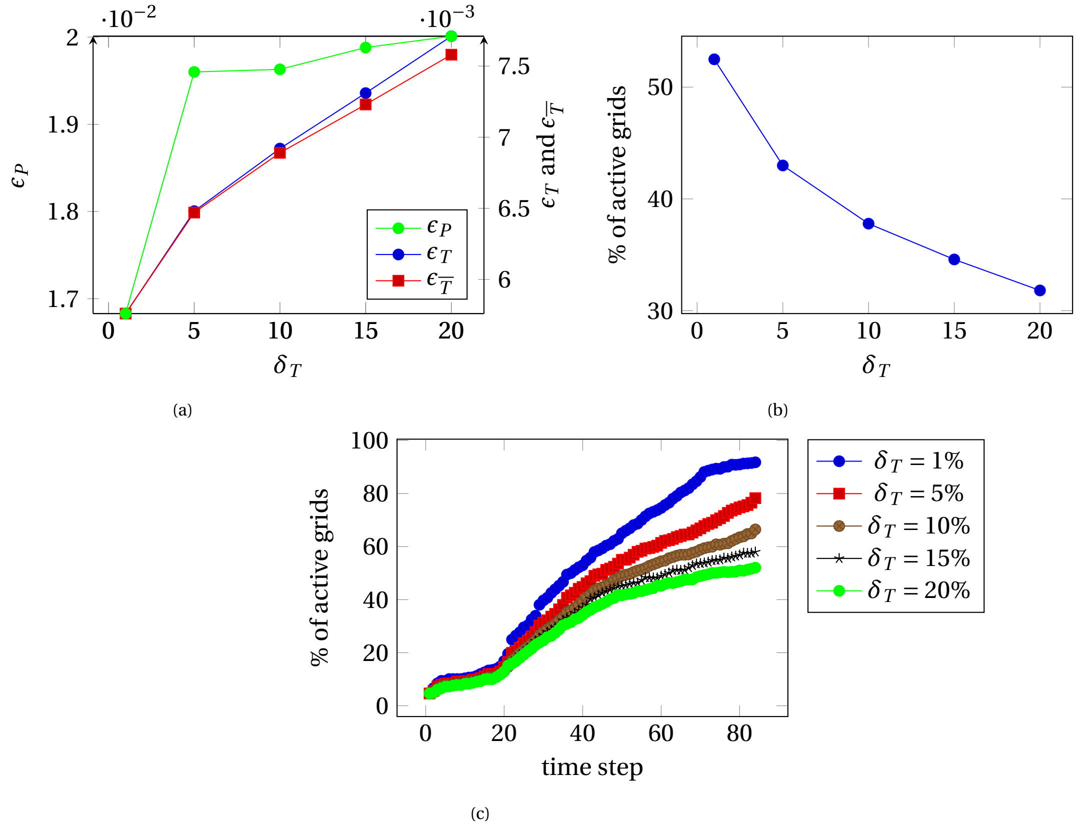

(a) (b)

(c)

Figure 5.18: Test Case 5 : Error of ADM solution with respect to fine-scale reference (a) and percentage of ADM active grids as function of ADM tolerance (b), and history of ADM grids during simulation (c).

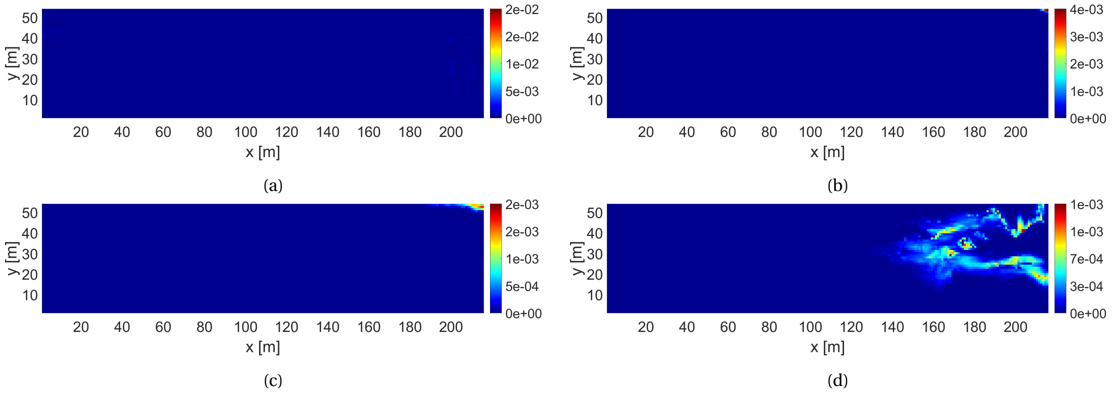

(a) (b)

(c) (d)

Figure 5.19: Test Case 5 : Absolute temperature difference of fluid and rock [K] after 0.01 (a), 0.1 (b), 1 (c), and 10 (d) days of injection.

6

Conclusion

In this thesis work, an ADM method for single-phase flow in geothermal reservoir is introduced. The coupling between mass and energy balance equations is treated using fully-implicit method to overcome strong coupling arising from compressible flow-heat system. Fine-scale solution is approximated using ADM method in order to find balance between efficiency (lower computational costs)on one side and accuracy on the other side. Note that despite allowing dynamic multilevel grid, fine-scale resolution is preserved on the area with significant physical changes for instance near the wells and temperature front. ADM method requires sequence of restriction and prolongation operators and assign them whenever and wherever fine-scale resolution is not needed. As a result, ADM method is capable to provide good fine-scale approximation with employment of only a fraction of fine-scale grids.

Numerical result for four different test cases in 2D reservoir are presented and compared with fine-scale solution used as reference. The sensitivities of error and number of active grids are also studied. Error grows larger proportionally with increase of ADM tolerance whereas number of active grids decreases with increase of ADM tolerance. Note that similar number of active grids are employed at the beginning of the simulation regardless of what ADM tolerance is employed.

Rarefaction or highly diffused temperature profile often leads to less number of fine-scale grids surrounding temperature front in large injection time. Note that despite non-thermal equilibrium, both fluid and rock temperature profile are quite close thus verifying thermal equilibrium assumption for flow inside matrix. Also note that despite its parabolic nature, rock temperature shows close-to-hyperbolic behavior due to the effect of massive fluid-rock heat exchange. Nonetheless, ADM method in non-thermal equilibrium geothermal reservoir has become powerful tool for real field geothermal simulation.

On the author's point of view, this work needs to be developed further by adding following ideas

1. One should introduce multiphase flow which allow phase change within geothermal reservoir. The importance of non-thermal equilibrium arises in the region where latent heat is collected to change fluid phase.

2. It is more favorable to add more physical complexity such as fracture network. On the area where fractures exist, rock has very limited time to heat the fluid up as the cold fluid is transported faster due to high flux velocities inside fractures.

3. One may consider solving geothermal formulation in dimensionless form. Strong flow-heat non-linearity leads to ill-conditioned Jacobian matrix and it is often difficult to solve. By employing dimensionless form, the problem is reduced to similar order of magnitude.

4. The advantage of employing ADM is its ability to preserve accuracy with considerably lower computational costs. As quantifying ADM error has been conducted in this thesis, the next step is to quantify ADM performance based on CPU time.

A

Fluid and Rock Properties

The following correlation describes simplified fluid model employed in numerical simulation. All units are subject to SI unit convention.

Fluid Properties

Fluid Density

Fluid density is described as function of pressure and temperature [46], and reads

$$\rho\,(P,T) = \rho_{fs}\,(T)\left[1 + c_f\,(T)\,(P - P_s)\right], \tag{A.1}$$

where saturation pressure P_s is fixed at constant 10^5 Pa, whereas fluid density at saturation condition ρ_s and fluid compressibility c_f are obtained from empirical correlation [37, 47]

$$\rho_s\,(T) = \begin{cases} -0.0032T^2 + 1.7508T + 757.5, & \text{if } T \leq 623.15\ K \\ -0.5214T^2 + 652.73T - 203714, & \text{if } T > 623.15\ K \end{cases}, \tag{A.2}$$

$$c_f\,(T) = \left(0.0839T^2 + 652.73T - 203714\right) \times 10^{-12}, \quad \text{for} \quad 273\ K < T < 647\ K\,. \tag{A.3}$$

Fluid Entalphy

Fluid enthalphy is described as function of pressure and temperature [46], and reads

$$h\,(P,T) = u_{ws} + C_p\,(T - T_s) + \frac{P}{\rho}, \tag{A.4}$$

where saturation temperature T_s is fixed at constant 373 K, fluid specific heat C_p is fixed at constant $4200\,\frac{J}{kg\cdot K}$ and fluid internal energy u_{ws} is fixed at $420000\,\frac{J}{kg}$.

Fluid Viscosity

Fluid viscosity is described as function of temperature [48], and reads

$$\mu\,(T) = 2.414 \times 10^{-5} \times 10^{\left(\frac{247.8}{T - 140}\right)}. \tag{A.5}$$

Rock Properties

Rock Porosity

Pore compressibility is defined as relative porosity change as a response of pressure change. Thus, relationship between porosity and pressure reads

$$\phi = \phi_0\,\exp\left[c_p\,(P - P_0)\right], \tag{A.6}$$

where ϕ_0 is porosity at initial pressure P_0, and c_p is user defined pore compressibility.

Rock-Fluid Heat Exchange Coefficient

Heat exchange between rock and fluid is described by a correlation established by [22, 40] which reads

$$Q_h = A\,U\left(T - \overline{T}\right), \tag{A.7}$$

where pore contact area A reads

$$A = \frac{6\left(1-\phi\right)}{D_p} \times V_B, \tag{A.8}$$

where V_B is bulk volume, and U is heat exchange coefficient between rock and fluid.

U in complex geometry is calculated using Nusselt number (N_u) which reads

$$\frac{1}{U} = \left(\frac{D_p}{N_u \cdot k_f} + \frac{D_p}{10 \cdot k_r}\right),$$

where D_p, k_f, and k_r represent representative pore diameter, fluid conductivity, and rock conductivity respectively.

Nusselt number (N_u) is calculated using empirical correlation [22, 40] and reads

$$N_u = \frac{1}{1-\phi} P_r^{0.33} R_e^{0.67}, \tag{A.9}$$

where Prandtl number (P_r) reads

$$P_r = \frac{C_p \mu}{k_f}. \tag{A.10}$$

Assuming non-Darcy flow in porous media is similar to flow in a conduit [49, 50], Reynold number (Re) reads

$$R_e = \frac{\rho\, v\, D_p}{\mu}, \tag{A.11}$$

where v is Darcy velocity.

Bibliography

[1] M. Cusini, C. van Kruijsdijk, and H. Hajibeygi, "Algebraic dynamic multilevel (adm) method for fully implicit simulations of multiphase flow in porous media," *Journal of Computational Physics*, vol. 314, pp. 60–79, 2016.

[2] J. Hansen, M. Sato, R. Ruedy, K. Lo, D. W. Lea, and M. Medina-Elizade, "Global temperature change," *Proceedings of the National Academy of Sciences*, vol. 103, no. 39, pp. 14288–14293, 2006.

[3] A. Shepherd and D. Wingham, "Recent sea-level contributions of the antarctic and greenland ice sheets," *science*, vol. 315, no. 5818, pp. 1529–1532, 2007.

[4] R. DeConto and D. Pollard, "Contribution of Antarctica to past and future sea-level rise," *Nature*, vol. 531, pp. 591–597, 3 2016.

[5] I. B. Fridleifsson, "Status of geothermal energy amongst the world's energy sources," *Geothermics*, vol. 32, pp. 379 – 388, 2003.

[6] "World Energy Resource: Geothermal," 2013.

[7] M. I. Komurcu and A. Akpınar, "Importance of geothermal energy and its environmental effects in Turkey," *Renewable Energy*, vol. 34, pp. 1611 – 1615, 2009.

[8] M. J. OSullivan, K. Pruess, and M. J. Lippmann, "State of the art of geothermal reservoir simulation," *Geothermics*, vol. 30, no. 4, pp. 395–429, 2001.

[9] R. Bertani, "Geothermal power generation in the world 2005-2010 update report," *Geothermics*, vol. 41, pp. 1–29, 2012.

[10] J. W. Lund, D. H. Freeston, and T. L. Boyd, "Direct utilization of geothermal energy 2010 worldwide review," *Geothermics*, vol. 40, no. 3, pp. 159–180, 2011.

[11] J. J. Mortensen, "Hot dry rock : A new geothermal energy source," *Energy*, vol. 3, pp. 639–644, 1978.

[12] D. E. White and D. L. Williams, "Assessment of geothermal resource of the united states - 1975," *Geological Survey Circular*, vol. 726, 1975.

[13] A. H. R. Iregui, P. Kruger, and A. London, "Analysis of heat transfer and energy recovery in fractured geothermal reservoir," *Stanford University*, vol. 31, 1978.

[14] F. H. Harlow and W. E. Pracht, "A theoretical study of geothermal energy extraction," *Journal of Geophysicla Research*, vol. 77, 1972.

[15] E. C. Aifantis and D. E. Beskos, "Heat extraction from hot dry rocks," *Mechanic Reseaarch Communication*, vol. 7, pp. 165–170, 1980.

[16] Z. Y. Wong, R. N. Horne, and H. A. Tchelepi, "Sequential implicit nonlinear solver for geothermal simulation," *Journal of Computational Physics*, vol. 368, pp. 236 – 253, 2018.

[17] M. Cusini, A. A. Lukyanov, J. Natvig, and H. Hajibeygi, "Constrained pressure residual multiscale (cpr-ms) method for fully implicit simulation of multiphase flow in porous media," *Journal of Computational Physics*, vol. 299, pp. 472–486, 2015.

[18] H. Liu, K. Wang, , and Z. Chen, "A family of constained pressure residual preconditioners for parallel reservoir simulation," in *Numerical Linear Algebra with Appllications*, pp. 120–146, 2015.

[19] M. HosseiniMehr, M. Cusini, C. Vuik, and H. Hajibeygi, "Algebraic dynamic multilevel method for embedded discrete fracture model (f-adm)," *Journal of Computational Physics*, vol. 373, pp. 324 – 345, 2018.

[20] J.-B. J. Fourier, *The analytical theory of heat.* Stechert, 1945.

[21] M. Kaviany, *Principle of Heat Transfer in Porous Media.* Springer, 1995.

[22] D. A. Nield and A. Bejan, *Convection in Porous Media.* Springer, 2006.

[23] P. Jenny, S. H. Lee, and H. A. Tchelepi, "Multi-scale finite-volume method for elliptic problems in subsurface flow simulation," *Journal of Computational Physics*, vol. 187, pp. 47–67, 2003.

[24] H. Zhou and H. Tchelepi, "Operator-Based Multiscale Method for Compressible Flow," *SPE Journal*, vol. 13, pp. 267 – 273, 2008.

[25] H. Hajibeygi, G. Bonfigli, M. Hesse, and P. Jenny, "Iterative multiscale finite-volume method," *Journal of Computational Physics*, vol. 227, pp. 8604–8621, 2008.

[26] M. Ţene, Y. Wang, and H. Hajibeygi, "Adaptive algebraic multiscale solver for compressible flow in heterogeneous porous media," *Journal of Computational Physics*, vol. 300, pp. 679–694, 2015.

[27] H. Hajibeygi and P. Jenny, "Multiscale finite-volume method for parabolic problems arising from compressible multiphase flow in porous media," *Journal of Computational Physics*, vol. 228, pp. 5129–5147, 2009.

[28] Y. Wang, H. Hajibeygi, and H. A. Tchelepi, "Algebraic multiscale solver for flow in heterogeneous porous media," *Journal of Computational Physics*, vol. 259, pp. 284–303, 2014.

[29] Y. Efendiev, T. Y. Hou, V. Ginting, *et al.*, "Multiscale finite element methods for nonlinear problems and their applications," *Communications in Mathematical Sciences*, vol. 2, no. 4, pp. 553–589, 2004.

[30] P. H. Sammon *et al.*, "Dynamic grid refinement and amalgamation for compositional simulation," in *SPE reservoir simulation symposium*, Society of Petroleum Engineers, 2003.

[31] D. W. Van Batenburg, A. De Zwart, P. M. Boerrigter, M. Bosch, and J. C. Vink, "Application of dynamic gridding techniques to ior/eor processes," in *IOR 2011-16th European Symposium on Improved Oil Recovery*, 2011.

[32] M. J. Berger and J. Oliger, "Adaptive mesh refinement for hyperbolic partial differential equations," *Journal of computational Physics*, vol. 53, no. 3, pp. 484–512, 1984.

[33] W. Mulder, R. Meyling, *et al.*, "Numerical simulation of two-phase flow using locally refined grids in three space dimensions," *SPE advanced technology series*, vol. 1, no. 01, pp. 36–41, 1993.

[34] E. Parramore, M. Edwards, M. Pal, and S. Lamine, "Multiscale finite-volume cvd-mpfa formulations on structured and unstructured grids," *Multiscale Modeling & Simulation*, vol. 14, pp. 559–594, 2016.

[35] S. Bosma, H. Hajibeygi, M. Tene, H. Tchelepi, *et al.*, "Multiscale finite volume method for discrete fracture modeling with unstructured grids," in *SPE Reservoir Simulation Conference*, Society of Petroleum Engineers, 2017.

[36] O. Moyner and K. Lie, "The multiscale finite-volume method on stratigraphic grids," *SPE J.*, vol. 19, no. 5, 2014, doi:10.2118/163649-PA.

[37] T. Praditia, R. Helmig, and H. Hajibeygi, "Multiscale formulation for coupled flow-heat equations arising from single-phase flow in fractured geothermal reservoirs," *Computational Geoscience*, vol. (in press), pp. DOI: 10.1007/s10596–018–9754–4, 2018.

[38] T. Praditia, "Multiscale Finite Volume Method for Coupled Single-Phase Flow and Heat Equations in Fractured Porous Media: Application to Geothermal System," Master's thesis, Delft University of Technology, 2017.

[39] D. W. Peaceman, "Interpretation of well-block pressures in numerical reservoir simulation," *SPE Journal*, vol. 18 (3), pp. 183–194, 1978.

[40] A. G. Dixon and D. L. Cresswell, "Theoretical Prediction of Effective Heat Transfer Parameters in Packed Beds," *The American Institute of Chemical Engineers*, vol. 25, pp. 663 – 675, 1979.

[41] J. Wallis, “Incomplete gaussian elimination as a preconditioning for generalized conjugate gradient acceleration,” *SPE Reservoir Simulation Symposium*, 1983.

[42] J. R. Wallis, R. P. Kendall, T. E. Little, and J. S. Nolen, “Constrained residual acceleration of conjugate residual methods,” *SPE Reservoir Simulation Symposium*, vol. doi:10.2118/13536-MS, 1985.

[43] H. Cao, H. A. Tchelepi, J. R. Wallis, and H. Yardumian, “Constrained residual acceleration of conjugate residual methods,” *SPE paper 96809, SPE Annual Technical Conference and Exhibition, Dallas, Texas, USA*, 2005.

[44] K. Stuben, T. Clees, H. klie, B. Lu, and M. Wheeler, “Algebraic multigrid methods (AMG) for the efficient solution of fully implicit formulations in reservoir simulation,” *SPE 105832, presented at the 2007 Reservoir Simulation Symposium*, 2007.

[45] R. Künze, I. Lunati, and S. H. Lee, “A multilevel multiscale finite-volume method,” *Journal of Computational Physics*, vol. 255, pp. 502–520, 2013.

[46] K. H. Coats, “Geothermal Reservoir Modelling,” in *SPE Annual Fall Technical Conference and Exhibition*, 1977.

[47] W. Wagner and H. Kretzschmar, *International Steam Tables - Properties of Water and Steam based on the Industrial Formulation IAPWS-IF97*. Springer, second ed., 2008.

[48] T.T. Al-Shemmeri, *Engineering Fluid Mechanics*, ch. 1, p. 18. Bookboon, 2012.

[49] T. H. Chilton and A. P. Colburn, “Pressure Drops in Packed Tubes,” *Industrial and Engineering Chemistry*, August 1931.

[50] Z. Zeng and R. Grigg, “A criterion for non-darcy flow in porous media,” *Transport in Porous Media*, vol. 63, pp. 57–69, 2006.